

Plasma Oscillation Characterization of NASA's HERMeS Hall Thruster via High Speed Imaging

Wensheng Huang*, Hani Kamhawi†, and Thomas W. Haag‡

National Aeronautics and Space Administration Glenn Research Center, Cleveland, OH, 44135, USA

The performance and facility effect characterization tests of NASA's 12.5-kW Hall Effect Rocket with Magnetic Shielding had been completed. As a part of these tests, three plasma oscillation characterization studies were performed to help determine operation settings and quantify margins. The studies included the magnetic field strength variation study, background pressure effect study, and cathode flow fraction study. Separate high-speed videos of the thruster including the cathode and of only the cathode were recorded. Breathing mode at 10-15 kHz and cathode gradient-driven mode at 60-75 kHz were observed. An additional high frequency (40-70 kHz) global oscillation mode with sinusoidal probability distribution function was identified.

Abbreviations

ARRM	= Asteroid Redirect Robotic Mission	JPL	= Jet Propulsion Laboratory
FECT	= Facility Effect Characterization Test	MCD	= Mean Channel Diameter
GRC	= Glenn Research Center	PCT	= Performance Characterization Test
HERMeS	= Hall Effect Rocket with Magnetic Shielding	SEP	= Solar Electric Propulsion
HSC	= High-Speed Camera	STMD	= Space Technology Mission Directorate
IPS	= Ion Propulsion System	TDM	= Technology Demonstration Mission
		TDU	= Technology Demonstration Unit

I. Introduction

FOR missions beyond low Earth orbit, spacecraft size and mass can be dominated by onboard chemical propulsion systems and propellants that may constitute more than 50 percent of the spacecraft mass. This impact can be substantially reduced through the utilization of Solar Electric Propulsion (SEP) due to its substantially higher specific impulse. Studies performed for NASA's Human Exploration and Operations Mission Directorate and Science Mission Directorate have shown that a 50kW-class SEP capability can be enabling for both near term and future architectures and science missions.¹ A high-power SEP element is integral to the Evolvable Mars Campaign, which presents an approach to establish an affordable evolutionary human exploration architecture. To enable SEP missions at the power levels required for these applications, an in-space demonstration of an operational 50kW-class SEP spacecraft has been proposed as a SEP Technology Demonstration Mission (TDM). In 2010 NASA's Space Technology Mission Directorate (STMD) began developing high-power electric propulsion technologies.^{2, 3} The maturation of these critical technologies has made mission concepts utilizing high-power SEP viable.

The Asteroid Redirect Robotic Mission (ARRM) is the leading candidate SEP TDM concept that utilizes an SEP spacecraft to return up to 20 metric tons of asteroidal mass from the surface of a larger asteroid, to a stable orbit around the Moon for subsequent access by a human crewed mission.⁴⁻⁷ The Ion Propulsion System (IPS) for ARRM will be used for heliocentric transfer from Earth to the target asteroid, orbit capture at the asteroid, transfer to a low orbit about the asteroid, a planetary defense demonstration after retrieval of the asteroidal mass from the larger asteroid, departure and escape from the asteroid, the heliocentric transfer from the asteroid to lunar orbit, and insertion into a lunar distant retrograde orbit. In addition, the IPS will provide pitch and yaw control of the spacecraft during IPS thrusting. To date, the technology development, performed by the NASA Glenn Research

* Propulsion Scientist, Electric Propulsion Systems, wensheng.huang@nasa.gov, Senior Member.

† Propulsion Scientist, Electric Propulsion Systems, hani.kamhawi-1@nasa.gov, Associate Fellow.

‡ Propulsion Scientist, Electric Propulsion Systems, thomas.w.haag@nasa.gov, Member.

Center (GRC) and the Jet Propulsion Laboratory (JPL), has been focused on an in-house effort to mature the high-power Hall thruster and power processing unit designs.

The high-power Hall thruster is referred to as the Hall Effect Rocket with Magnetic Shielding (HERMeS). In addition to making ARRM viable, the HERMeS propulsion system also has potential commercial applications for raising the orbit of next generation, higher power communication satellites from low-Earth orbit (LEO) to geosynchronous Earth orbit (GEO).

To meet the requirements of the mission concepts under development, the capabilities of the 12.5-kW HERMeS will be enhanced relative to the current state of the art. Characteristics of the thruster include high system efficiency ($\geq 57\%$), high specific impulse (up to 3000 s), and high propellant throughput capability (3400 kg). Additionally, HERMeS was designed to deliver similar system efficiency at a more modest specific impulse of 2000 seconds. High specific impulse operation supports mission concepts with high total-impulse requirements like ARRM, while the modest specific impulse operation is beneficial for time-critical operations like LEO to GEO orbit raising.

To verify that the 12.5-kW HERMeS meets the established requirements and to reduce several key risks associated with the thruster, a series of tests are being performed on two Technology Development Units (TDUs). The testing methodology for many of these tests will form the basis for the acceptance and qualification tests of the flight version of the thruster. Figure 1 shows a diagram of the testing on the HERMeS TDUs thus far as well as tests that are planned. Testing that has been completed include the propellant uniformity test⁸, magnetic shielding characterization test⁹, performance characterization test (PCT)¹⁰, thermal characterization test (TCT)¹¹, facility effect characterization test (FECT)¹⁰, and electrical configuration characterization test¹². The PCT, TCT, and FECT were performed with a single test setup.

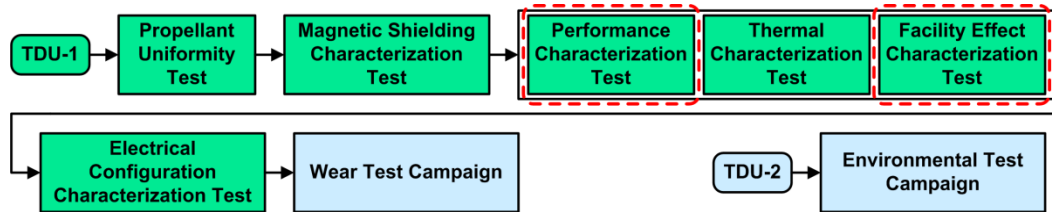


Figure 1. A diagram of the TDU test campaign.

This paper will focus on the plasma oscillation studies that were parts of the PCT and FECT, which were performed on the TDU1 at NASA GRC. The main purpose of the plasma oscillation studies were to supply the oscillation data needed to determine the operational settings and quantify the margins associated with the throttling points of the HERMeS TDU. These settings and margins in turn contributed to a primary objective of the PCT, which was to determine the performance of the thruster. Three plasma oscillation studies that deployed high-speed imaging were performed. The magnetic field strength variation study focused on determining the nominal magnetic coil settings and the amount of magnetic field strength margin available. The background pressure effect study focused on changes in plasma oscillation characteristics as the background pressure varied, which helped determine the maximum background pressure for future testing. The cathode flow fraction study focused on changes in plasma oscillation characteristics as the cathode flow fraction varied, which helped quantify cathode flow fraction margins. The background pressure effect study is described in detail in a companion paper.¹³ Relevant background pressure effect results are reproduced here for reference.

The remainder of the paper describes the relevant background information, test setup, analysis approach, results, and conclusions.

II. Background

Many kinds of plasma oscillations have been known to exist in Hall thrusters.¹⁴ Since the 1960's, numerous studies have been performed to characterize these oscillations.¹⁵⁻²⁹ In the current generation of Hall thrusters, there are three oscillation modes that dominate the oscillation spectra, the breathing mode, the spokes mode, and the cathode gradient-driven mode. Recent studies have shown that for magnetically-shielded Hall thrusters the breathing mode tend to dominate while the spoke mode is only present at very high magnetic field strength.³⁰

The breathing and spoke modes are believed to be tied to ionization processes in the Hall thruster because their frequencies are in the kilohertz to tens of kilohertz range, which is most closely related to the characteristic ion and neutral transit time across the discharge zone.^{14, 20}

The breathing mode oscillation is believed to be an axial ionization wave. The name comes from the resemblance of the exhausted plasma packets to breaths of gas. The simplest quantitative description of the

breathing mode oscillation is based on modeling work done by Fife. Fife started with the assumption that the breathing mode is an axial ionization-driven oscillation and derived the scaling relationship shown in Eq. (1) below.²⁰

$$2\pi f_i = \frac{\sqrt{u_i u_n}}{L_i} \quad (1)$$

In Eq. (1), f_i is the frequency of the breathing mode, u_i is the speed of the ions leaving the thruster, u_n is the speed of the neutrals entering the ionization zone, and L_i is the characteristic length over which the oscillation action is taking place. Typically, L_i is taken to be the length of the ionization zone. This scaling relationship has been shown to predict general trends in the breathing mode oscillation frequency with discharge voltage though the exact values do not always agree.²⁰ The role of the breathing mode in electron transport is currently unclear, though Lobbia has argued that the breathing mode is an intrinsic feature in the Hall thruster and is necessary for the thruster to achieve enough electron transport to maintain the discharge.²⁵

The spokes mode oscillation is believed to be an azimuthal ionization wave. The name comes from the appearance of rotating plasma packets, which resemble spokes on a wheel, in the discharge channel of a Hall thruster when viewed from downstream of the exit plane. Works performed by Janes and Lowder¹⁵ and McDonald²⁷ have provided some basic understanding of the spokes mode oscillation. The spokes mode is presented as an alternate means by which electron current can be transported across magnetic field lines. Subsequent work by Sekerak showed that a non-magnetically-shielded Hall thruster can operate with almost no breathing mode and strong spokes mode oscillations present. Sekerak observed that the presence of spokes mode without breathing mode is correlated with high thrust efficiency for a medium-power Hall thruster.²⁸ Hara and Sekerak then deployed a hybrid-direct kinetic simulation to model the transition between breathing and spokes mode.²⁹ Spokes have been observed to travel in the same direction as the Hall current and anywhere from two to six spokes can be observed simultaneously.^{27, 28}

The cathode gradient-mode was discovered much more recently compared to the two aforementioned modes. Jorns and Hofer found light structure that resembles a single spoke emanating from the cathode rotating at high frequencies (70-90 kHz) when studying the H6MS Hall thruster.³¹ They discovered that the rotating structure is a type of instability driven by density gradient just downstream of the cathode and built a complete theoretical description of the instability.³¹

III. Experimental Setup

To simplify plot labeling, throttle points are labeled as vvv-k.k, where vvv is the discharge voltage in volts, and k.k is the discharge power in kilowatts. For the magnetic field strength variation study, the operating points are labeled as vvv-k.k-Mb.bb where b.bb is the normalized magnetic field strength. Magnetic field strength is normalized by the maximum magnetic field strength tested. For example B0.33 is a low magnetic field strength, 0.66 is a moderate field strength, and 1.00 is a high field strength. For the background pressure effect study, the operating points are labeled as vvv-k.k-Pnx where n is the normalized background pressure, defined as the number of multiples of the lowest achievable operating background pressure for the throttle point vvv-k.k. For the cathode flow fraction study, the operating points are labeled as vvv-k.k-cfmm where mm is the cathode flow fraction in percentage.

Unless otherwise noted, all spatial positions presented in this paper have been normalized by the mean channel diameter (MCD) of the thruster. MCD is defined as the average of the inner and outer discharge-channel wall diameters. Furthermore, thruster-centric azimuthal coordinate, ϕ , was defined as 0° at the 12 o'clock position (vertically the highest point of the discharge channel). The azimuthal angle increases in the clock-wise direction when viewing the thruster from a downstream position. For example, an azimuthal angle of 90° corresponded to the 3 o'clock position.

A. Thrusters and Test Matrix

The HERMeS TDU1 was designed to be a 12.5 kW, 3000 s, magnetically-shielded Hall thruster. The thruster had been operated over discharge voltages ranging from 300 to 800 V, corresponding to a specific impulse range of 2000 to 3000 s at full power. The thruster had also been power throttled over discharge powers ranging from 0.6 to 12.5 kW.¹⁰ Figure 2 shows a picture of the NASA HERMeS TDU1 with various test equipment.

Thruster magnet coils were energized so that the magnetic shielding topology was always maintained. The only degree of freedom in the magnetic field setting was the strength of the magnetic field. Peak radial magnetic field strength along the discharge channel centerline was chosen as the reference when referring to the strength of the magnetic field.

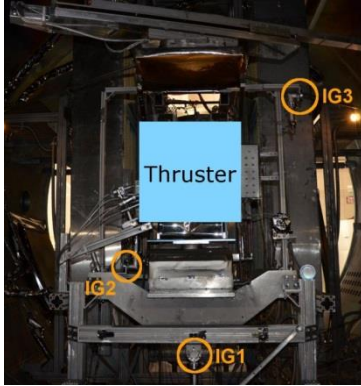


Figure 2. NASA HERMeS TDU1 and nearby ion gauges.

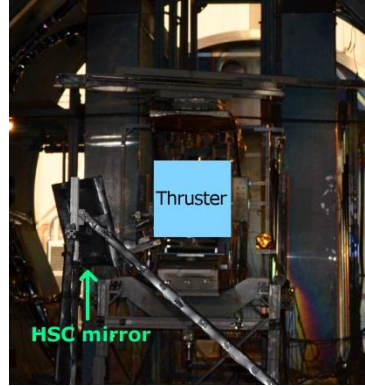


Figure 3. NASA HERMeS TDU1 and the HSC mirror.

Table 1. Table of thruster throttle points.

Label	Discharge voltage, V	Discharge power, kW
300-4.7	300	4.7
300-9.4	300	9.4
400-12.5	400	12.5
500-12.5	500	12.5
600-12.5	600	12.5
700-12.5	700	12.5
800-9.7	800	9.7
800-12.5	800	12.5

For the purpose of PCT and FECT, eight thruster throttling points were selected. These throttle points are listed in Table 1. To determine a set of nominal operating parameters for each throttle point, the background pressure was set to lowest achievable and the cathode flow fraction was set to 7% (i.e. cathode mass flow rate was set to 7% of the anode mass flow rate). The nominal magnetic field strength was then determined by maximizing thruster efficiency while maintaining a reasonable amount of magnetic field strength margin (>25 gauss) against oscillation mode transitions. The mass flow rates that gave the correct discharge power for the given throttle point was recorded as the nominal mass flow rates.

During the magnetic field strength variation study, the background pressure was set to the lowest achievable and the cathode flow fraction was set to 7%. The anode mass flow rate was fixed at the nominal value of each throttle point. Only the magnetic field strength was varied.

During the background pressure effect study, the magnetic field strength was set to the nominal value for a given throttle point. The background pressure was raised by injecting xenon via an auxiliary flow line that exits at >4 meters downstream of the thruster pointed away from the thruster. Mass flow rates were then adjusted to maintain the same discharge power as background pressure varied.

During the cathode flow fraction study, the magnetic field strength and anode mass flow rate were set to the nominal values for a given throttle point. The background pressure was set to lowest achievable. The cathode flow fraction was varied over the range of 4% to 9%. The cathode flow fraction study was performed for only the 300 V and 800 V throttle points.

B. Test Facility

Testing was performed in Vacuum Facility 5 (VF5) at NASA GRC. This cylindrical facility is 4.6 m in diameter, 18.3 m long, and was evacuated with a set of cryo-panels. The thruster was mounted on a thrust stand located close to the cryo-panels, with the thruster firing away from the panels. Background pressure near the thruster was monitored with three ion gauges. Figure 2 shows the positions of the three ion gauges relative to the thruster. Note that ion gauge #1 points downstream while ion gauges #2 and #3 points away from the thruster towards the cylindrical walls of the facility. Correction of gauge readings for effective sensor sensitivity was obtained by calibrating the ion gauges against a spinning rotor gauge in a controlled setup using research grade xenon. Correction of gauge readings for effects of local temperature and direction of the gauge openings relative to the background flux were obtained through a series of modeling studies and verified by experimental data.³² The ion gauge studies also showed that pointing the ion gauge opening orthogonal to the firing axis provides the most accurate measurement of the local static pressure. Based on these studies, ion gauges #2 and #3 were selected for calculating the local back pressure experienced by the thruster. After the aforementioned corrections, the remaining uncertainty in the calculated pressure was dominated by ion gauge electrical and electronic noise. These remaining uncertainties were estimated by the manufacturer to be $\pm 6\%$ of the reading. The lowest pressure achieved for the tested throttle points varied from 3.0×10^{-6} to 6.3×10^{-6} Torr.

Research-grade xenon propellant was supplied via commercially available mass flow controllers to the thruster, cathode, and auxiliary flow line. These mass flow controllers were calibrated using research-grade xenon prior to testing. Typical uncertainty of mass flow rate measurement was $\pm 1\%$ of reading.

Electrical power was supplied to the thruster with commercially available power supplies. Separate power supplies supported the main discharge, cathode heater, keeper, inner magnet, and outer magnet. An electrical filter was placed between the thruster and the discharge power supply. All power supplies and the filter were located outside of the vacuum facility.

C. High-Speed Camera

A high-speed camera (HSC) was deployed to study the oscillation characteristics of the thruster. The HSC was mounted outside of the vacuum facility looking through a window at a mirror inside the vacuum facility. The mirror was a second surface mirror mounted at an angle far downstream of the thruster to reflect light from the thruster to the HSC. The mirror was situated just below the centerline of the vacuum facility to allow an infrared camera mounted downstream of the mirror to have direct line-of-sight to the thruster. Use of the infrared camera was described in a separate publication.¹¹ The mounting structure for the HSC was shielded with Grafoil to reduce the amount of backspattered material. Figure 3 shows a photograph of the HERMeS TDU1 on the thrust stand in the background with the HSC mirror in the foreground. Figure 4 shows a diagram of the experimental setup inside the vacuum facility.

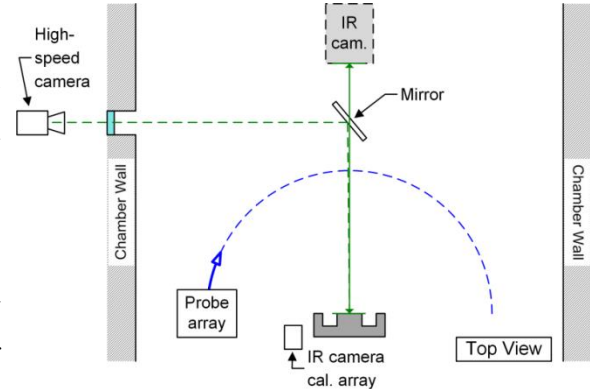


Figure 4. Diagram of the experimental setup inside the vacuum facility.

Three current probes were also installed on the discharge electrical line to provide time-resolved data on the discharge current. These probes were connected to an oscilloscope, which recorded the data. Current probes were placed both upstream and downstream of the electrical filter on the discharge line. Data from the probe downstream of the electrical filter, which is just upstream of the thruster, were compared to the HSC data. The power spectra from the current probe and the HSC analysis were found to be nearly identical.

IV. Experimental Data Analysis

Two types of HSC video were taken. For the thruster HSC videos, the video frame enclosed the entire discharge channel and the frame rate was 180 kfps. For the cathode HSC videos, the video frame enclosed only the cathode and the frame rate was 480 kfps.

The HSC data were processed through a series of steps listed below.

1. The video was averaged over time to create an averaged image.
2. A series of fits were performed on the averaged image to find the center of the thruster and the boundaries of the discharge. Light from the cathode was excluded.
3. The data within the discharge region was divided into 120 azimuthal bins and the average intensity in each bin on each frame was calculated. This binned data was then normalized against the time-averaged values of the binned data. The azimuthal angles of the bins were corrected based on an image calibration performed prior to evacuation of the vacuum facility. Thus, the fact that the HSC image was seen through a mirror situated below the centerline of the vacuum facility was corrected for.
4. A statistical analysis was performed to determine the probability distribution function (PDF) of the intensity.
5. A two-dimensional (2D) Fourier transform was performed to obtain a series of power spectra categorized by the mode number m .
6. The results were plotted against magnetic field strength, background pressure, and cathode flow fraction.

Figure 5 an example of a thruster HSC video being analyzed. The left image is the averaged image and the right image shows how the program divided up the image at step three. A dashed green line radiating from the center of the thruster indicates the $\phi = 0^\circ$ position on the actual thruster. A small green branch perpendicular to the dashed green line points in the actual clock-wise direction. Recall HSC recorded images that were reflected through a mirror. The small red circle indicates a region encompassing the cathode that is excluded from the analysis. Two concentric green circles that sandwich a region highlighted in red indicate the boundaries of the discharge.

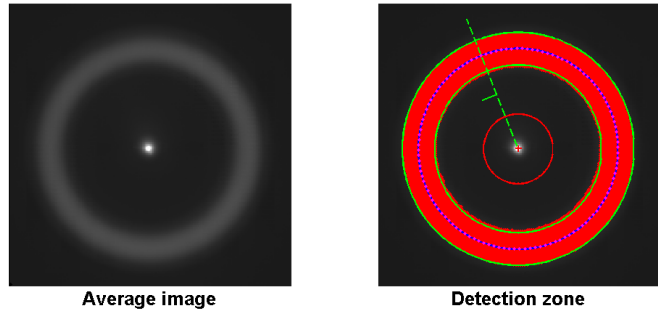


Figure 5. Example of thruster HSC video analysis.

The data resulting from analysis step three were the relative fluctuation of each azimuthal bin with time. This step produced results that were much less sensitive to variations in pixel sensitivity, transmission of the viewport, and reflectance of the mirror. Note that step three also removed any real, time-averaged, azimuthal variation in light intensity. For instance, the presence of a stationary hot spot would be removed by this step. This characteristic was considered acceptable because the present study was focused on transient instead of stationary features.

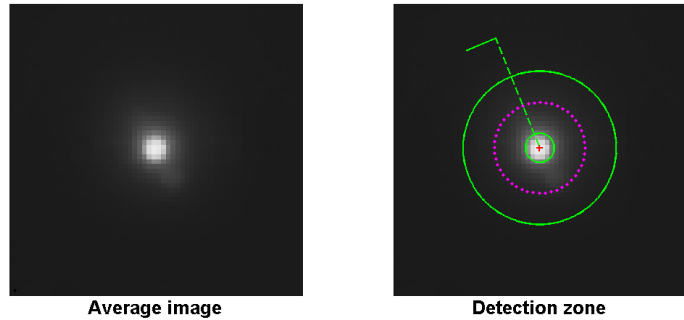


Figure 6. Example of cathode HSC video analysis.

For the power spectra obtained from analysis step five, the $m = 0$ (zeroth order) spectrum showed the frequency of any oscillation modes where the entire discharge plasma oscillated together. This phenomenon is referred to as global oscillation. The $m = 1$ (first order) spectrum showed the frequency of any spokes mode with one spoke present, the $m = 2$ spectrum showed the frequency of any spokes mode with two spokes present, and so on.

During this study, the team discovered that the main discharge of the HERMeS TDU1 did not exhibit spokes mode behavior except at one operating condition with high magnetic field strength. Given a lack of spokes mode, this paper will focus on the global oscillation modes that were present. A previous publication describes the details regarding the subtlety of analyzing 2D Fourier transform results when spokes are present.³³

Analysis of the global oscillation modes can also be completed by averaging the light intensity data across all bins and performing a 1D Fourier transform. This approach was also performed and the results checked against the $m = 0$ spectrum from 2D Fourier transform. The two approaches were in excellent agreement.

Analysis procedure of the cathode videos was very similar to the analysis of the thruster videos with two important differences. The first difference was that instead of analyzing the discharge channel, cathode HSC analysis focused on the region near the cathode and excluded a very small spot right at the center of the cathode that tended to saturate the HSC sensor. The second difference was that 48 azimuthal bins were used instead of 120 due to the reduction in the number of pixels available per unit azimuthal angle. Figure 6 shows an example of a cathode HSC video being analyzed.

Unlike the thruster videos, the cathode videos exhibited strong $m = 1$ oscillations that corresponded to the gradient-driven mode unique to centrally mounted cathode in a Hall thruster, which were first identified and described by Jorns.³¹ For this reason, both $m = 0$ and $m = 1$ power spectra were of note for the cathode videos.

V. Experimental Results

A. General Results

Figures 7 to 9 show several examples of phi-t diagrams from thruster HSC analysis. A phi-t diagram is the equivalent of an x-t diagram for visualizing traveling waves in a cylindrical or spherical coordinate system. The horizontal axis is the azimuthal angle and the vertical axis is time. Red pixels represent high light intensity and blue pixels represent low light intensity. These figures illustrate that the discharge channel of the HERMeS TDU1 exhibited mostly global mode oscillation. The lone exception was the 300-4.7-M1.00 (high magnetic field strength) operating condition. Figures 7 and 8 are examples of phi-t diagrams where only global modes are present. Since the

horizontal axis is azimuthal angle, presence of horizontal bands implies the entire discharge channel was oscillating together. Figure 9 shows the phi-t diagram of the 300-4.7-M1.00 operating condition where a single spoke was present. On a phi-t diagram, spokes mode show up as diagonal bands because the angular position of spokes changes with time.

In contrast, Figs. 10 to 12 show several examples of phi-t diagrams from cathode HSC analysis. Diagonal bands are clearly visible in these and other cathode phi-t diagrams indicating the presence of a strong $m = 1$ mode that corresponds to the cathode gradient-driven mode.

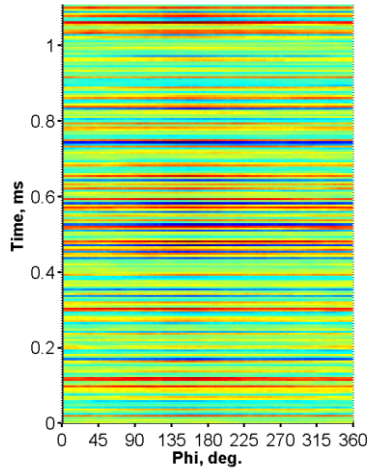


Figure 7. Thruster phi-t diagram for 300-9.4-P1X.

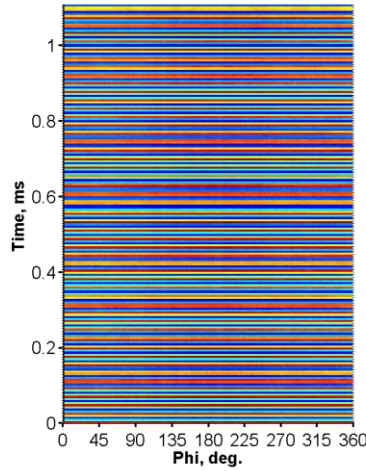


Figure 8. Thruster phi-t diagram for 600-12.5-P1X.

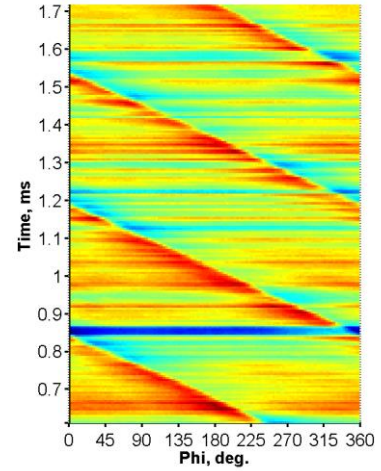


Figure 9. Thruster phi-t diagram for 300-4.7-M1.00.

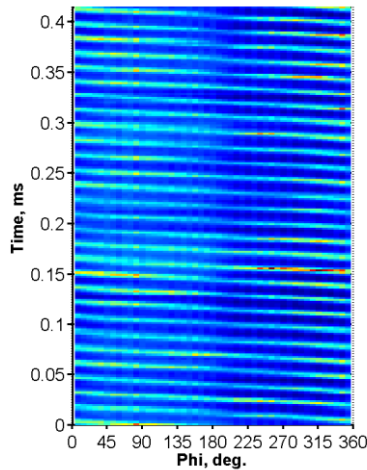


Figure 10. Cathode phi-t diagram for 300-9.4-P1X.

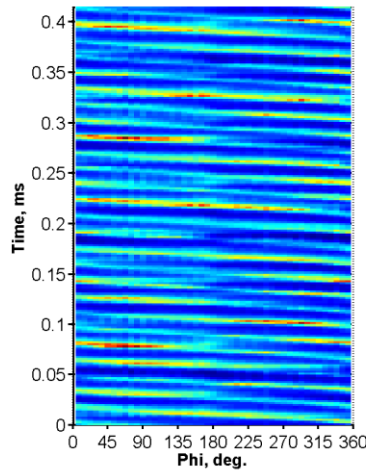


Figure 11. Cathode phi-t diagram for 600-12.5-P1X.

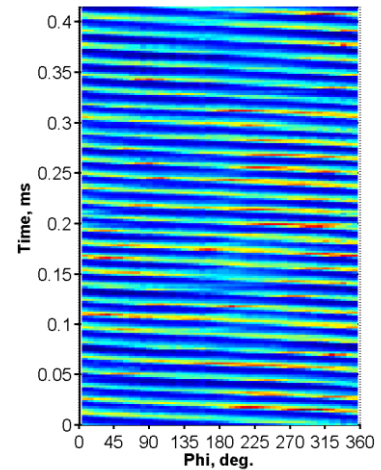


Figure 12. Cathode phi-t diagram for 300-4.7-M1.00.

To better visualize trends in the oscillation modes with background pressure, a series of PDFs of the light intensity were generated. A PDF of light intensity is a good way to visualize how often the thruster is bright as opposed to dark as well as how bright and how dark the plasma gets. Different types of plasma oscillations have different PDF characteristics. For example, a truly random oscillation process exhibits a Gaussian PDF distribution while a purely sinusoidal oscillation process exhibits a unique two-peak PDF distribution. For the collected data set, cathode PDFs displayed similar shapes as the corresponding thruster PDFs except where noted.

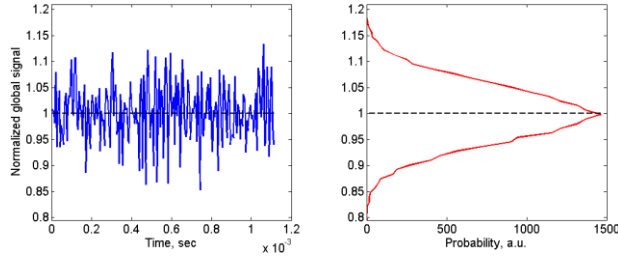


Figure 13. Thruster intensity (left) and probability distribution function (right) for 300-9.4-P1X.

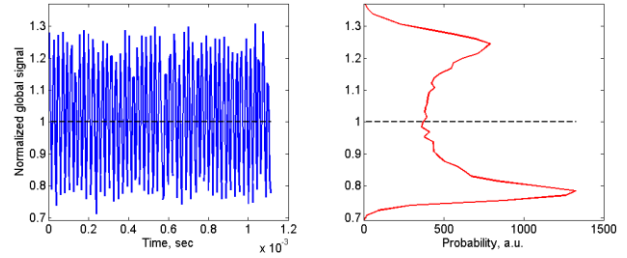


Figure 14. Thruster intensity (left) and probability distribution function (right) for 600-12.5-P1X.

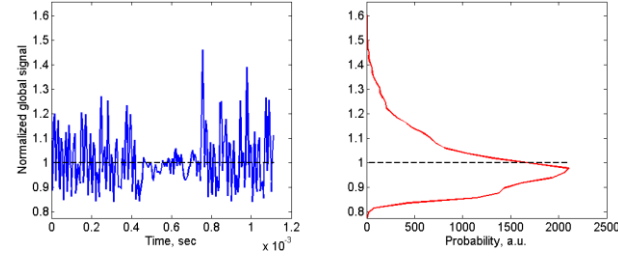


Figure 15. Thruster intensity (left) and probability distribution function (right) for 800-12.5-P1X.

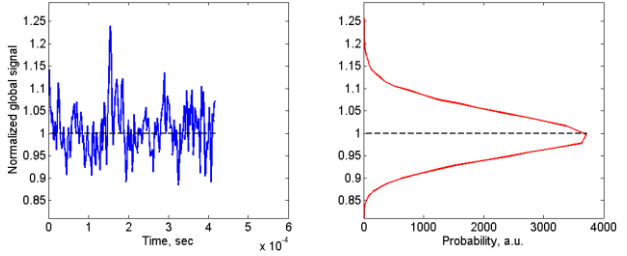


Figure 16. Cathode intensity (left) and probability distribution function (right) for 300-9.4-P1X.

Figures 13 to 15 show examples of different patterns of global oscillations observed in the discharge channel during testing. The left sub-plot of each figure shows a snippet of the light intensity as a function of time. The right sub-plot shows the associated PDF. Figure 13 shows an example of a PDF with Gaussian shape where the light intensity appeared to oscillate randomly. Figure 14 shows an example of a PDF with a unique two-peak shape that was only seen when the oscillation was purely sinusoidal. Figure 15 shows an example of a PDF with a skewed shape. A skewed PDF was found to be associated with a discharge that periodically flared to high intensities for very brief durations and was at a low intensity most of the time. Figure 16 shows an example of the pattern observed in the plasma near the cathode during testing. Figures 13 and 16 together illustrate the similarity in the PDFs between the thruster and cathode videos for most operating condition.

Figures 17 and 18 show examples of thruster light intensity power spectra observed during testing. The $M = 0$ spectra corresponded to global oscillations and dominated the spectra for all tested throttle points. Figures 19 and 20 show examples of cathode light intensity power spectra observed during testing. Generally speaking, the $M = 0$ cathode spectra matched the corresponding thruster spectra.

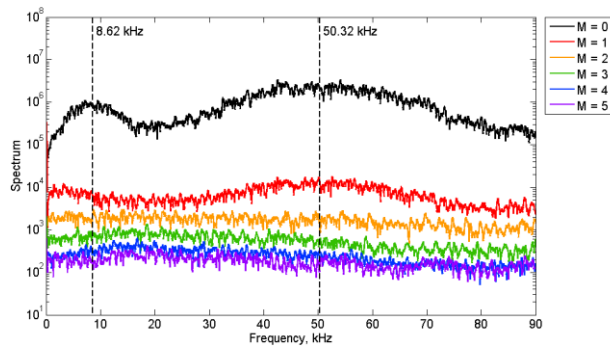


Figure 17. Thruster light intensity power spectra for 300-9.4-P1X.

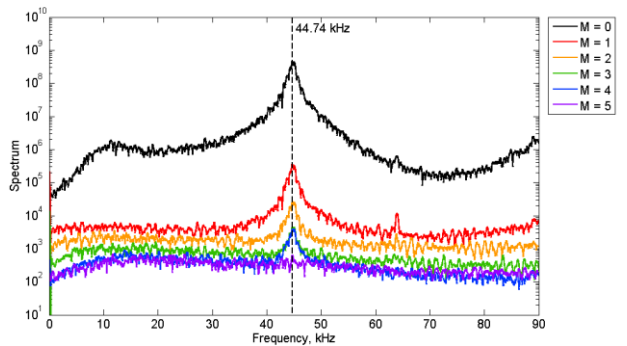


Figure 18. Thruster light intensity power spectra for 600-12.5-P1X.

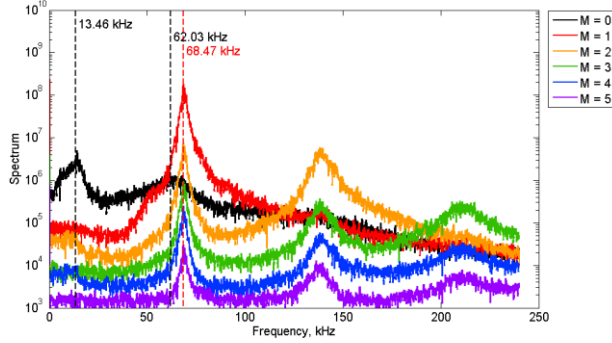


Figure 19. Cathode light intensity power spectra for 300-9.4-P1X.

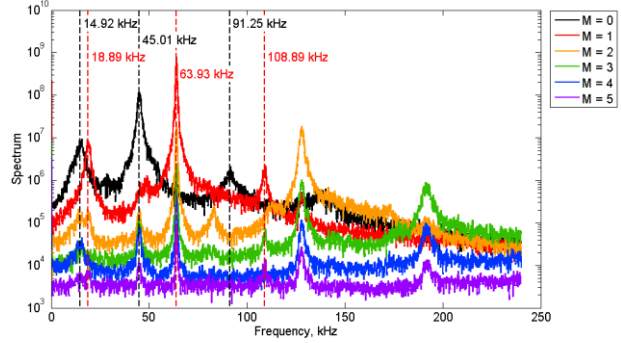


Figure 20. Cathode light intensity power spectra for 600-12.5-P1X.

From Figures 17 and 18, one can see that there were both low frequency (10-15 kHz) and high frequency (40-70 kHz) global oscillation occurring in the discharge channel. For a few of the conditions, there were also low amplitude harmonics of the main peaks present. From Figures 19 and 20, one can see the presence of cathode gradient-driven mode (60-75 kHz, $m=1$) previously described in Section II.

To gain a better understanding of the nature of the global oscillation modes present in the discharge channel, a cross-correlation study involving the PDF and power spectra data was performed. Operating conditions were categorized under one of three types according to their PDFs: Gaussian, Skewed, or Sinusoid. Operating conditions were also categorized under one of three categories according to their power spectra: low frequency peak only, high frequency peak only, low and high frequency peaks present. Table 2 summarizes the results of the correlation study. The percentage in each cell is the percent of total number of operating conditions that fall under the associated category. For example, 21% of the operating conditions studied with the HSC had sinusoidal PDFs and high frequency global oscillation. The sample size of the study was 68. From this table, one can see that sinusoidal PDFs were predominately associated with high frequency global oscillation modes while skewed PDFs were predominately associated with low frequency global oscillation modes. Gaussian PDFs were associated with both low and high frequency oscillation modes. The frequency, PDF, and location of the low frequency Gaussian mode suggest that it is the breathing mode described in Section II. The high frequency global oscillation mode with a sinusoidal PDF does not appear to match any oscillation mode previously described in the literature and may be unique to magnetically-shielded Hall thrusters and/or central mounting of the cathode. There were also high frequency Gaussian oscillations present that may or may not be related to either the breathing mode or the high frequency sinusoidal mode. The nature of the high frequency Gaussian mode requires further investigation.

Table 2. Result of cross correlation study involving thruster PDF and power spectra data.

	Gaussian	Skewed	Sinusoid
Low freq. only	10%	21%	2%
High freq. only	13%	3%	21%
Low and high freq.	10%	15%	5%

B. Magnetic Field Strength Variation Study

To determine how the oscillation characteristics changed with magnetic field strength a number of color contour plots were generated. Figures 21 to 23 show representative contour plots of the PDFs of the thruster light intensity as the magnetic field strength varied. In PDF contour plots, red represents high probability, blue represents low probability, and a pair of dashed lines indicate the approximate boundaries the light intensity. The dashed lines were calculated by determining where the PDF dropped below 1% of maximum probability.

Figure 21 illustrates a common feature found in the magnetic field strength variation study, which is that the PDF became skewed and the magnitude of oscillation became high at low magnetic field strength. All throttle points exhibited this behavior at sufficiently low magnetic field strength. The transition from typical oscillation amplitude to very large oscillation amplitude occurs over small changes in magnetic field strength, on the order of a few tens of Gauss. While the maximum tested magnetic field strength was the same for all throttle points, the minimum tested magnetic field strength depended on when the large amplitude oscillation started to occur. When the magnetic field strength was low enough to trigger large amplitude oscillation, the discharge current was found to rise noticeably over time and temperatures measured by thruster thermocouples were found to rise very quickly. We determined that the aforementioned large amplitude oscillation can potentially damage the thruster so we never allowed the thruster to dwell long at very low magnetic field strength. The cut off on the left side of each contour plot represents

the lowest magnetic field strength that was operated for each throttle point. When the magnetic field strength was not low, the PDFs and the oscillation amplitude were fairly constant across a large range of field strength. This behavior is very useful for a Hall thruster as it allows operators to pick nominal operating field strength with large margins against unstable thruster operation.

Figure 22 illustrates another common feature discovered in the magnetic field strength variation study. At high discharge voltage (500 to 800 V), the PDF of thruster light intensity switched into and out of the high-frequency sinusoidal oscillation mode depending on the magnetic field strength. The only common trend between the throttle points that displayed sinusoidal PDFs is that the sinusoidal PDF disappears at low magnetic field strength. For some throttle points, disappearance of sinusoidal PDF at high magnetic field strength was also observed.

Table 3 summarizes the range of magnetic field strength over which sinusoidal PDFs were observed. The oscillation amplitude of the thruster in high-frequency sinusoidal mode was observed to be higher than when the thruster was in quiescent breathing mode (e.g. 300-9.4 with moderate magnetic field strength) but much lower than when the magnetic field strength was too low. The team tentatively concluded that the oscillation amplitude associated with high-frequency sinusoidal mode was not so high as to put undue burden on the electrical filtering circuit.

Figure 23 shows the unique case of the 800-12.5 throttle point where the PDF was mostly skewed but a sinusoidal PDF made a brief appearance at around a normalized magnetic field strength of 0.66. Moreover, unlike the other tested throttle points, there was a region of heightened oscillation amplitude at normalized magnetic field strength of 0.5 to 0.7. No conclusion has been drawn about whether operation in this region of heightened oscillation amplitude is problematic in the long term.

Another unique case was the 800-9.7 throttle point where the minimum normalized magnetic field strength needed to sustain the discharge was 0.58, well in excess of the ~ 0.4 value found for the other throttle points. The 800-9.7 throttle point also exhibited large amplitude skewed PDF at very high magnetic field strength.

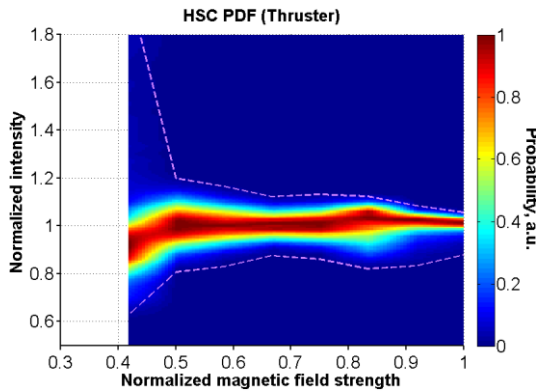


Figure 21. PDF of thruster light intensity as magnetic field strength varied for the 300-9.4 throttle point.

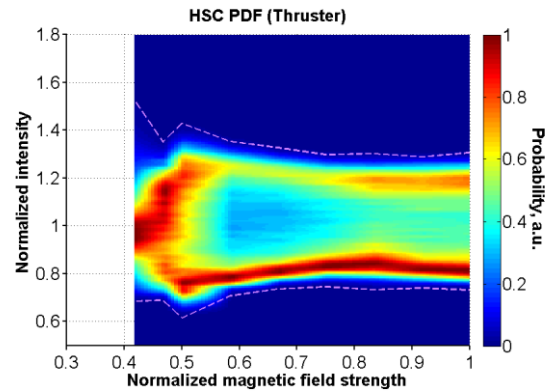


Figure 22. PDF of the thruster light intensity as magnetic field strength varied for the 600-12.5 throttle point.

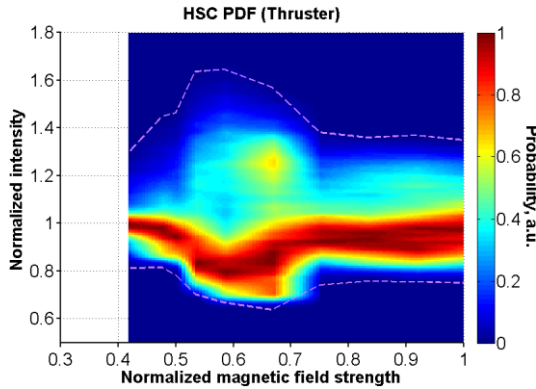


Figure 23. PDF of the thruster light intensity as magnetic field strength varied for the 800-12.5 throttle point.

Table 3. Range of magnetic field strength over which sinusoidal PDFs were observed

Throttle point	Range of magnetic field strength
300-4.7	none
300-9.4	none
400-12.5	none
500-12.5	0.80-1.00
600-12.5	0.50-1.00
700-12.5	0.55-0.65
800-9.7	none
800-12.5	0.66

Figures 24 and 25 show two representative contour plots of the $m = 0$ power spectra of the thruster light intensity as the magnetic field strength varied. In power spectra contours, yellowish white represents peaks and dark red represents trough. The color bar is on a base-10 decibel scale so a difference of 10 on the color bar is a factor of 10 in the absolute magnitude of the spectral power. Due to limited magnetic field strength resolution, the peaks will sometime take on a banded appearance. The discrete-band appearance is an artifact. The frequencies of the real peaks are generally continuous functions of magnetic field strength.

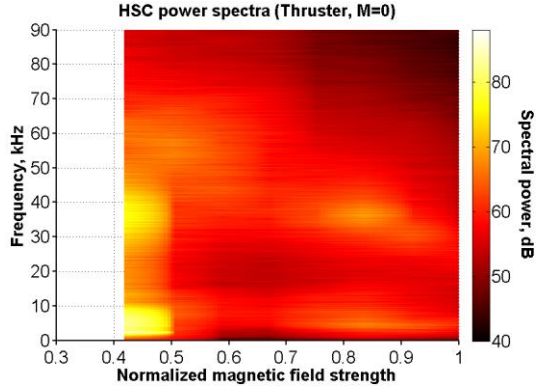


Figure 24. The $m=0$ power spectra of the thruster light intensity as magnetic field strength varied for the 300-9.4 throttle point.

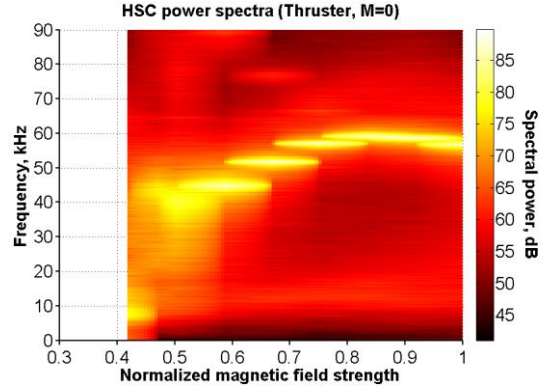


Figure 25. The $m=0$ power spectra of the thruster light intensity as magnetic field strength varied for the 600-12.5 throttle point.

Figure 24 is of the 300-9.4 throttle point and represents the trend exhibited at many throttle point, which was that the power spectra showed intense breathing oscillation at low magnetic field strength but was relatively quiescent everywhere else. The frequency of the breathing mode appeared to decrease slightly as the magnetic field strength increased. Figure 25 is of the 600-12.5 throttle point and represents the type of power spectra contour associated with the high-frequency sinusoidal mode. The frequency of the high frequency peak was decreasing with increasing magnetic field strength for the 500-12.5 throttle point but was increasing with increasing magnetic field strength for the 600-12.5 and 700-12.5 throttle points.

Figures 26 and 27 show two representative contour plots of the PDFs of the cathode light intensity as the magnetic field strength varied. These illustrate an interesting phenomenon. For throttle points where the low amplitude breathing mode dominated the discharge channel, the thruster and cathode exhibited nearly identical PDF trends (compare Figs. 21 and 26). For throttle points where the high-frequency sinusoidal mode dominated the discharge channel, the cathode exhibited characteristics of both sinusoidal and skewed PDFs (compare Figs. 22 and 27).

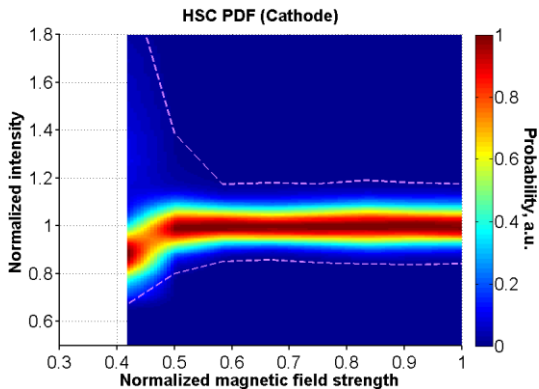


Figure 26. PDF of cathode light intensity as magnetic field strength varied for the 300-9.4 throttle point.

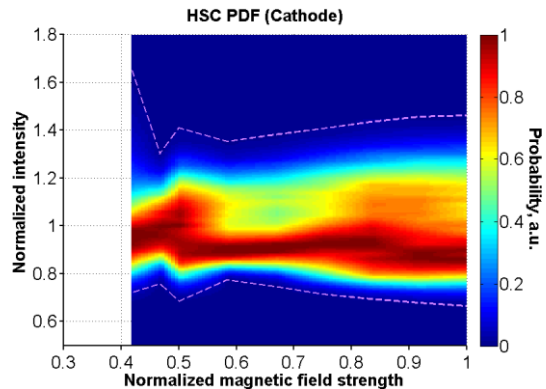


Figure 27. PDF of cathode light intensity as magnetic field strength varied for the 600-12.5 throttle point.

Figures 28 and 29 show two representative contour plots of the $m = 1$ power spectra of the cathode light intensity as the magnetic field strength varied. Recall that the $m = 0$ power spectra of the thruster and cathode were nearly

identical. For the low discharge voltage throttle points, represented in Fig. 28, the frequency of the cathode gradient-driven mode increased with increasing magnetic field strength. For the high discharge voltage throttle points, represented in Fig. 29, the frequency of the cathode gradient-driven mode was largely constant with increasing magnetic field strength.

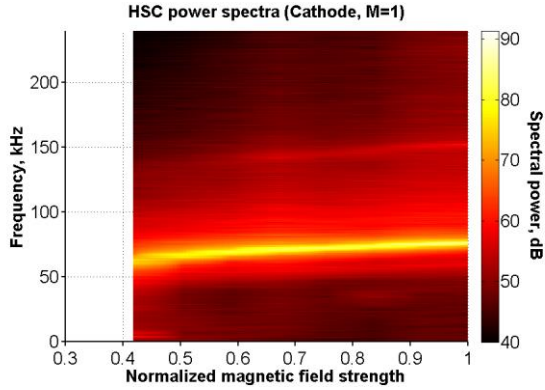


Figure 28. The $m=1$ power spectra of the cathode light intensity as magnetic field strength varied for the 300-9.4 throttle point.

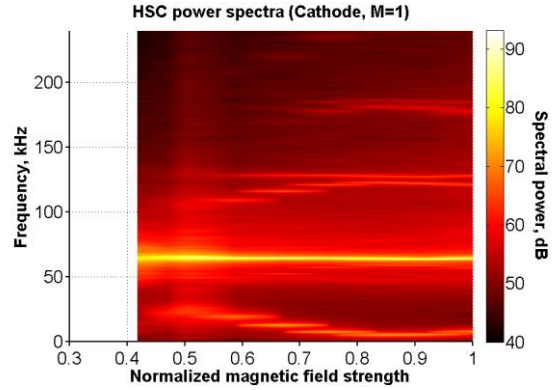


Figure 29. The $m=1$ power spectra of the cathode light intensity as magnetic field strength varied for the 600-12.5 throttle point.

Tables 4 and 5 summarize the general trend of the thruster and cathode light characteristics as functions of magnetic field strength, respectively. The overall conclusion from the magnetic field strength variation study was that the HERMeS TDU1 exhibited stable operation over large ranges of magnetic field strength except when operating at 800 V. For the 800-9.7 throttle point, the range of magnetic field strength over which stable operation was achieved was less than half the range found in other throttle points. For the 800-12.5 throttle point, there was a

Table 4. General trend of the thruster PDF and power spectra with increasing magnetic field strength.

Throttle point	Trend in PDF	Trend in $m=0$ power spectra*
300-4.7	Low amplitude Gaussian	Unique behavior
300-9.4	Low amplitude Gaussian	8.6 kHz \rightarrow 4.9 kHz
400-12.5	Low amplitude Gaussian	10.8 kHz \rightarrow 4.1 kHz
500-12.5	Moderate amplitude Gaussian \rightarrow Sinusoidal	53.5 kHz \rightarrow 58.9 kHz \rightarrow 37.4 kHz
600-12.5	Sinusoidal	46.8 kHz \rightarrow 50.3 kHz \rightarrow 34.3 kHz
700-12.5	Sinusoidal \rightarrow Skewed	42.8 kHz \rightarrow 59.1 kHz \rightarrow 56.7 kHz
800-9.7	Moderate amplitude Gaussian \rightarrow Skewed	48.4 kHz \rightarrow 68.9 kHz \rightarrow 66.7 kHz
800-12.5	Skewed \rightarrow Sinusoidal/Skewed \rightarrow Skewed	48.4 kHz \rightarrow 68.9 kHz \rightarrow 66.7 kHz
	All are high amplitude Skewed at very low magnetic field strength	Unique behavior

Table 5. General trend of the cathode PDF and power spectra with increasing magnetic field strength.

Throttle point	Trend in PDF	Trend in $m=1$ power spectra*
300-4.7	Low amplitude Gaussian	51.5 kHz \rightarrow 71.5 kHz
300-9.4	Low amplitude Gaussian	62.5 kHz \rightarrow 76 kHz
400-12.5	Low amplitude Gaussian	59 kHz \rightarrow 74 kHz
500-12.5	Moderate amplitude Gaussian	65.5 kHz \rightarrow 68 kHz
600-12.5	Sinusoidal/Skewed	constant
700-12.5	Skewed	62 kHz \rightarrow 65 kHz
800-9.7	Skewed	69 kHz \rightarrow 66 kHz
800-12.5	Skewed \rightarrow Sinusoidal/Skewed \rightarrow Skewed	63 kHz \rightarrow 60.5 kHz \rightarrow 65.5 kHz
	All are high amplitude Skewed at very low magnetic field strength	

*Frequency trend with two numbers indicate monotonic increase or decrease. Frequency trend with three numbers indicate an increase follow by a decrease or a decrease follow by an increase.

region of heightened oscillation amplitude at normalized magnetic field strength of 0.5 to 0.7. The latest ARRM throttle curve no longer include 800 V throttle points.³⁴

Full sets of contour plots can be found in the appendix. Figures 35 to 42 show the contour plots of the PDFs of the thruster light intensity as the magnetic field strength varied for all throttle points. Figures 43 to 50 show the contour plots of the $m = 0$ power spectra of the thruster light intensity as the magnetic field strength varied. Figures 51 to 58 show the contour plots of the $m = 1$ power spectra of the cathode light intensity as the magnetic field strength varied.

C. Background Pressure Effect Study

As with the magnetic field strength study, a number of color contours were generated to help visualize the trend in the PDF and power spectra as the background pressure varied. Figures 30 and 31 show two representative contour plots of the PDFs of the thruster light intensity as the background pressure varied. Figure 30 is of the 300-9.4 throttle point and represents the basic trend exhibited by most throttle point, which was that the PDF did not change meaningfully as the background pressure varied. Figure 31 is of the 800-12.5 throttle point and is unique in that the PDF became more skewed as the background pressure was increased.

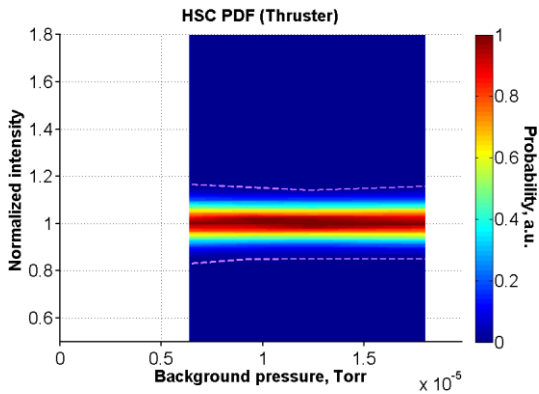


Figure 30. PDF of the thruster light intensity as background pressure varied for the 300-9.4 throttle point.

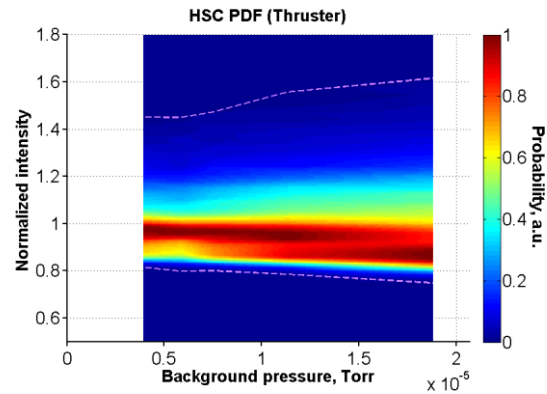


Figure 31. PDF of the thruster light intensity as background pressure varied for the 800-12.5 throttle point.

Figures 32 and 33 show two representative contour plots of the $m = 0$ power spectra of the thruster light intensity as the background pressure varied. Figure 32 is of the 500-12.5 throttle point and represents the trend exhibited at most throttle point, which was that the power spectra did not change meaningfully as the background pressure varied. Figure 33 is of the 600-12.5 throttle point and represents the trend exhibited at three throttle points where the high frequency peak increased in frequency with background pressure.

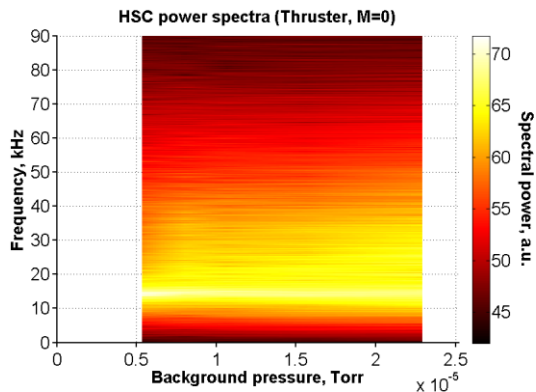


Figure 32. The $m=0$ power spectra of the thruster light intensity as background pressure varied for the 500-12.5 throttle point.

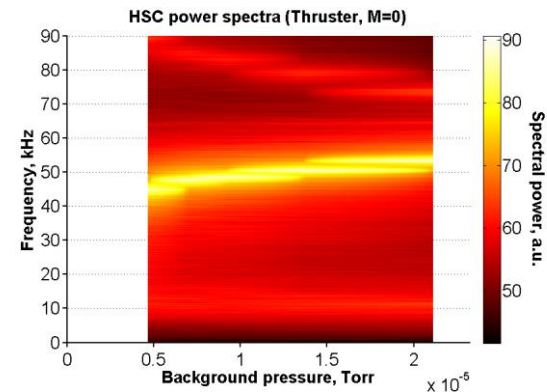


Figure 33. The $m=0$ power spectra of the thruster light intensity as background pressure varied for the 600-12.5 throttle point.

PDFs and $m = 0$ power spectra of the cathode light matches those of the thruster except where the thruster displayed sinusoidal PDF the cathode displayed skewed PDF, same as what was found in the magnetic field strength variation study. The $m = 1$ power spectra of the cathode light showed that the cathode gradient-driven mode was constant as background pressure rose.

Table 6 summarizes the general trend of the thruster PDF and power spectra as functions of background pressure. This table shows that there were some differences in behavior at different throttle points. However, the PDFs did not change from one type to another with varying background pressure and the same spectral peaks were present at different background pressure, implying that the oscillation mode of thruster did not change over the range of background pressure tested.

Table 6. General trend of the thruster PDF and power spectra with increasing background pressure.

Throttle point	Trend in PDF	Trend in $m=0$ power spectra
300-4.7	Constant	10 kHz \rightarrow 11.4 kHz
300-9.4	Constant	Low-freq.: constant High-freq.: 50.3 kHz \rightarrow 65.4 kHz
400-12.5	Constant	Low-freq.: constant High-freq.: 53.5 kHz \rightarrow 60.6 kHz
500-12.5	Constant	Constant
600-12.5	Constant	44.7 kHz \rightarrow 53.3 kHz
700-12.5	Nearly constant	Constant
800-9.7	Constant	Constant
800-12.5	Increasingly skewed	Low-freq.: 8.7 kHz \rightarrow 9.8 kHz High-freq.: 54.3 kHz \rightarrow 50.4 kHz

Implications of the background pressure effect study for the FECT as well as full sets of contour plots can be found in another publication.¹³

D. Cathode Flow Fraction Study

Recall that the cathode flow fraction study was only performed for the 300 V and 800 V throttle points. As with the other two studies, color contour plots were made for the cathode flow fraction study. PDFs of the thruster and cathode light were largely constant with varying cathode flow fraction. The lone exception was the PDF of the thruster light for the 300-9.4 throttle point where the amplitude of the oscillation increased with cathode flow fraction. The $m = 0$ power spectra for the thruster and cathode were in excellent agreement. Note that the cathode gradient-driven mode sometimes showed up in the $m = 0$ power spectra of the cathode, and more rarely in the $m = 0$ power spectra of the thruster. The associated peaks were always very low in amplitude, implying the cathode gradient-driven mode was localized to the vicinity of the cathode. The $m = 1$ power spectra for the cathode showed that the frequency of the cathode gradient-driven mode decreased with increasing cathode flow fraction. Figure 34 show a contour plot of the $m = 1$ power spectra of the cathode light illustrating the aforementioned trend.

The conclusion from the cathode flow fraction study was that the thruster was stable over a wide range of cathode flow fraction and an appropriate amount of margin can be applied without issues.

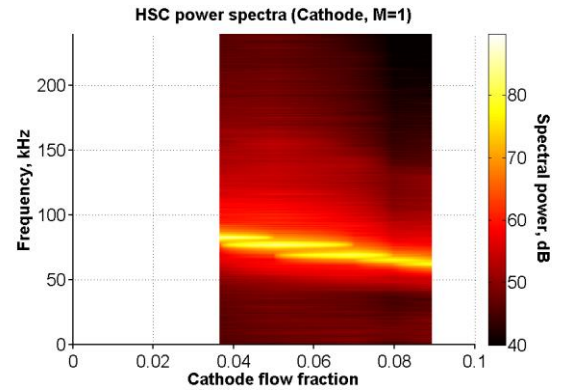


Figure 34. The $m=1$ power spectra of the cathode light intensity as cathode flow fraction varied for the 300-9.4 throttle point.

VI. Discussions

The previous section discussed results as they applied to the objectives of the HERMeS TDU test campaign. This section will focus more on discoveries from the HSC studies that are of scientific value.

A. General Trends

Table 7. General trends for the identified oscillation modes.* V_d = discharge voltage, ω = frequency

Mode	Trend with increasing magnetic field strength	Trend with increasing background pressure	Trend with increasing cathode flow fraction
Breathing	Low V_d : ω decreased High V_d : when present, ω constant or increased	Low V_d : ω slightly increased High V_d : ω mostly constant	Constant
Cathode Gradient-Driven	Low V_d : ω increased High V_d : ω constant	Constant	ω decreased
High-Freq. Sinusoidal	High V_d only; ω decreased for 500-12.5; ω increased then plateaued for 600-12.5 and 700-12.5; see Table 3	ω increased for 600-12.5; ω slightly decreased for 700-12.5	No example

Table 7 summarizes the trends discovered in the three HSC studies as they pertained to each of the three oscillation modes identified. A common trend shown in this table is that there were distinct differences in oscillation behavior between when the thruster operated at low discharge voltage (approximately 300-500 V) and at high discharge voltage (approximately 500-800 V). This change in behavior was likely related to the fact that the breathing mode dominated the discharge for low discharge voltage conditions while the high-frequency sinusoidal mode showed up for high discharge voltage conditions.

When the breathing mode dominated the discharge (low discharge voltage), the breathing mode frequency decreased with increasing magnetic field strength. Of the variables present in Eq. (1) only the ionization zone length was directly affected by the magnetic field strength. The implication is that increasing magnetic field strength caused the ionization zone length to increase, which caused the breathing mode frequency to decrease. However, the frequency changed by a factor of about two over the tested range, implying the ionization length changed by the same factor. Whether the change in magnetic field strength can really cause such a large change in ionization zone length is unclear. The assumptions associated with Eq. (1) could have been broken over such a large range in magnetic field strength.

Frequency of the breathing mode increased slightly with rising background pressure. This phenomenon can be explained by the past observation that increasing background pressure caused the discharge to recede into the discharge channel, which was likely associated with a decrease in ionization zone length.²⁶ Since the increase in frequency was small (~15%) the change in ionization zone length was likely small.

Characteristics of the breathing mode exhibited no noticeable change with cathode flow fraction. This behavior was expected since the cathode was stable over the range of tested cathode flow fractions. The small changes in cathode mass flow was unlikely to affect an oscillation mode drive by discharge channel ionization physics.

The frequency of the cathode gradient-driven mode increased with magnetic field strength for low discharge voltage conditions. This behavior was predicted by Jorns and Hofer in a sensitivity study using a physical model of this oscillation mode.³¹ For high discharge voltage conditions, the frequency of the cathode gradient-driven mode was largely constant with changing magnetic field strength. Competing factors like changing electron temperature may be at work.

The characteristics of the cathode gradient-driven mode were largely constant with changing background pressure. One possible implication is that a centrally mounted cathode is not susceptible to background pressure effects. Changes in thruster characteristics with background pressure observed in the FECT were likely due to actions relating to the discharge channel.¹³

The frequency of the cathode gradient-driven mode decreased with increasing cathode flow fraction. Increasing cathode flow decreases the local electron temperature by increasing the electron-neutral collision frequency. According to sensitivity study by Jorns and Hofer³¹, reduction in electron temperature leads to a decrease in wave frequency, which matches the observed trend.

The high-frequency sinusoidal mode exhibited rather complex behavior with changing magnetic field strength. At first glance, the frequency exhibited both increasing and decreasing behavior depending on the discharge voltage. One possibility is that the frequency maximized at different magnetic field strength for different discharge voltage. For example, for the 500-12.5 throttle point, there appeared to be a maximum in frequency for this mode at a normalized magnetic field strength of ~0.7. For the 600-12.5 and 700-12.5 throttle points, the maximum appeared at normalized magnetic field strength of ~0.85. The fact that the frequency had maximum values as the magnetic field strength varied may suggest competing effects were at work for this oscillation mode.

The background pressure effect study contained only two throttle points at which the discharge exhibited high-frequency sinusoidal mode. The behavior of this mode for the two throttle points were not the same. We cannot draw any generalized conclusions regarding the behavior of the high-frequency sinusoidal mode with changing background pressure.

Similarly, no generalized conclusions can be made about how the high-frequency sinusoidal mode varies with cathode flow fraction. Though as with the breathing mode, there is no reason to believe that the tested range of cathode flow fraction would have a noticeable effect on the high-frequency sinusoidal mode.

B. High-Frequency Sinusoidal Mode

The team's initial hypothesis for the high-frequency sinusoidal mode was that they were excited by the cathode gradient-driven mode. However, a close examination of the power spectra, which is summarized in Tables 4 and 5, revealed that the two modes exhibited different frequencies for a wide variety of operating conditions. Furthermore, Table 7 shows that the high-frequency sinusoidal mode and the cathode gradient-driven mode exhibited very different trends with changing control parameters.

Another hypothesis was that the high-frequency sinusoidal mode is another form of the breathing mode. Based on the frequency of this sinusoidal mode (40-75 kHz), the underlying mechanic is likely related to electron-neutral interactions (e.g. ionization and excitation), which would indeed make it similar to the breathing mode. However, Table 7 shows that the sinusoidal mode has a noticeably different relationship with the magnetic field strength than the breathing mode. Additionally, the sinusoidal PDF displayed by the high-frequency sinusoidal mode implies this mode is associated with undamped harmonic oscillation while the breathing mode is associated with Gaussian PDF as a result of turbulent action.

For the time being no conclusion is drawn about the underlying physics of the high-frequency sinusoidal mode. The unique characteristics of this mode do not match any other modes currently described in the literature. The high-frequency sinusoidal mode may be unique to magnetically-shielded Hall thrusters. For example, the great reduction in plasma-wall interaction associated with magnetically-shielded Hall thruster may have reduced damping associated with the interaction enough to allow this harmonic oscillation to propagate. Alternately, this mode may have existed all along in other Hall thruster and had simply escaped notice because researchers had not previously focused on the PDFs of plasma oscillations.

VII. Conclusions

Three HSC studies were performed on the HERMeS TDU1 to satisfy the objectives of the PCT and FECT. Results from the magnetic field strength variation and cathode flow fraction studies helped determine the nominal magnetic field strength, cathode flow fraction, and related margins for operating the TDU1. Results from the background pressure effect study helped determine the maximum background pressure in which future HERMeS testing should be carried out.

Combining the results of all three studies revealed a number of interesting findings regarding plasma oscillations in the HERMeS TDU1. Spokes mode oscillation was found to be largely absent. Trends in the behavior of the breathing mode and cathode gradient-driven mode largely matched current theories. A new high-frequency sinusoidal mode was discovered that does not match any oscillation mode previously described in the literature. Further analysis is needed to uncover the underlying physical nature of the newly discovered oscillation mode.

Appendix

Figures 35 to 42 show the contour plots of the PDFs of the thruster light intensity as the magnetic field strength varied.

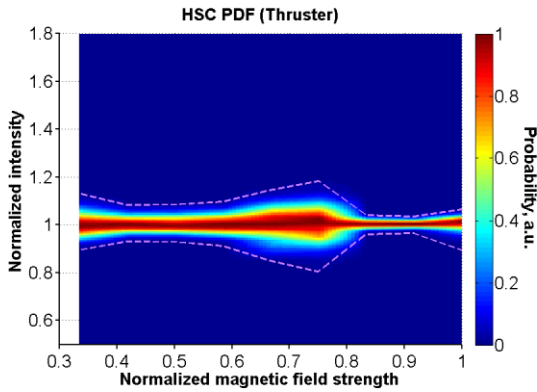


Figure 35. PDF of the thruster light intensity as magnetic field strength varied for the 300-4.7 throttle point.

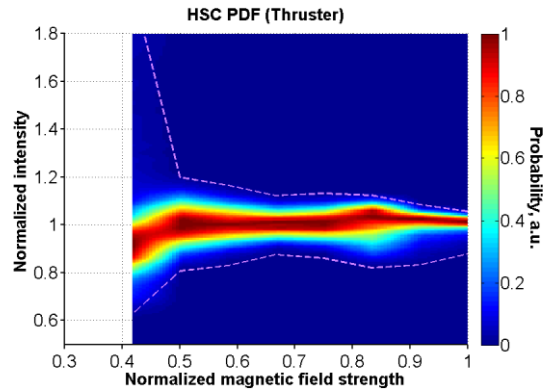


Figure 36. PDF of thruster light intensity as magnetic field strength varied for the 300-9.4 throttle point.

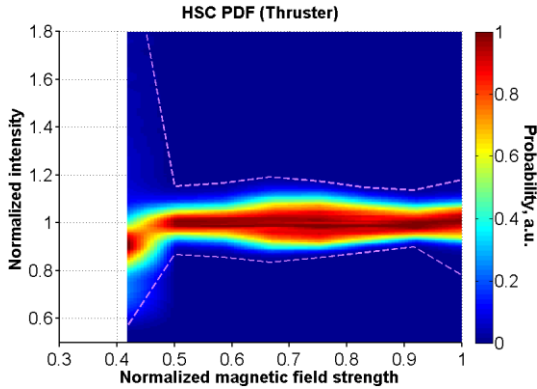


Figure 37. PDF of thruster light intensity as magnetic field strength varied for the 400-12.5 throttle point.

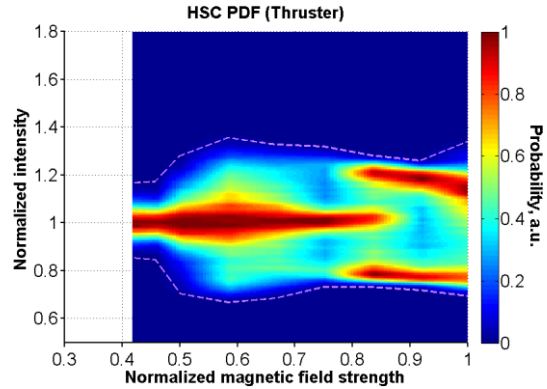


Figure 38. PDF of thruster light intensity as magnetic field strength varied for the 500-12.5 throttle point.

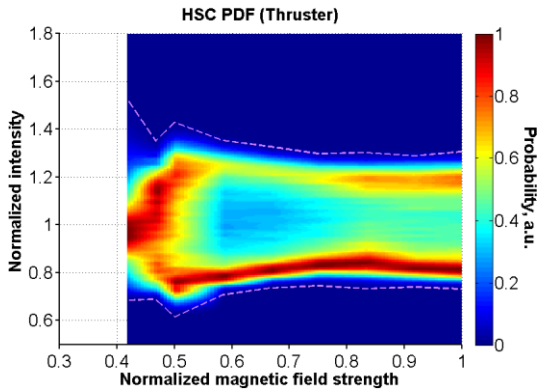


Figure 39. PDF of thruster light intensity as magnetic field strength varied for the 600-12.5 throttle point.

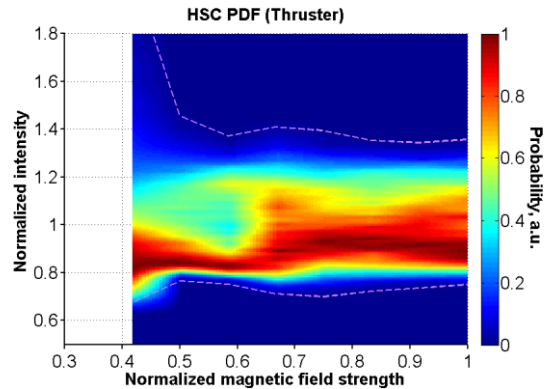


Figure 40. PDF of thruster light intensity as magnetic field strength varied for the 700-12.5 throttle point.

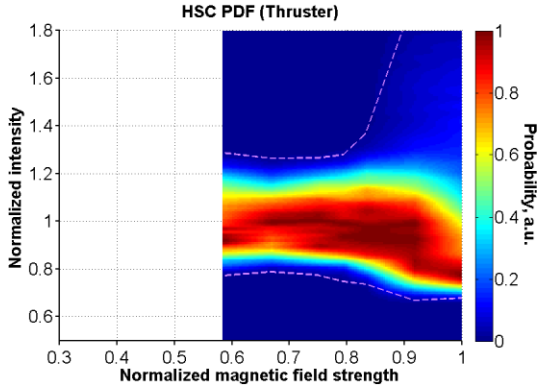


Figure 41. PDF of thruster light intensity as magnetic field strength varied for the 800-9.7 throttle point.

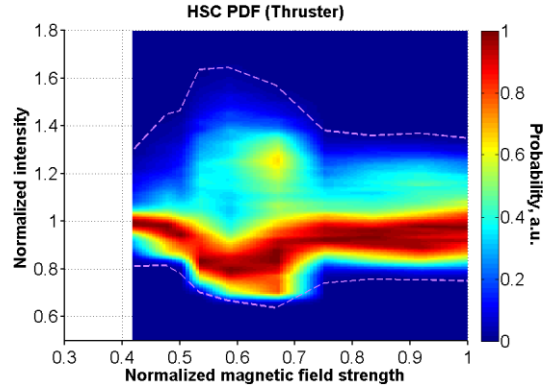


Figure 42. PDF of thruster light intensity as magnetic field strength varied for the 800-12.5 throttle point.

Figures 43 to 50 show the contour plots of the $m = 0$ power spectra of the thruster light intensity as the magnetic field strength varied.

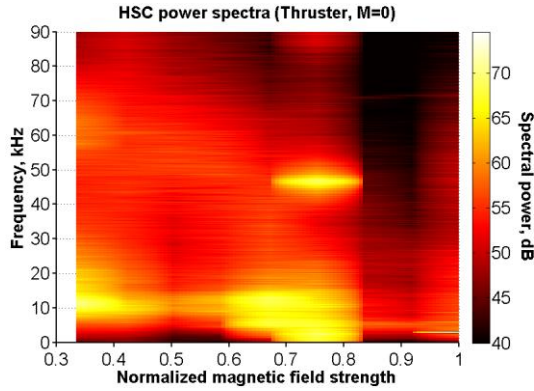


Figure 43. The $m=0$ power spectra of the thruster light intensity as magnetic field strength varied for the 300-4.7 throttle point.

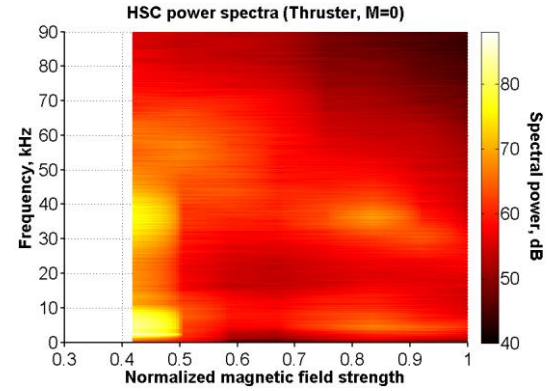


Figure 44. The $m=0$ power spectra of the thruster light intensity as magnetic field strength varied for the 300-9.4 throttle point.

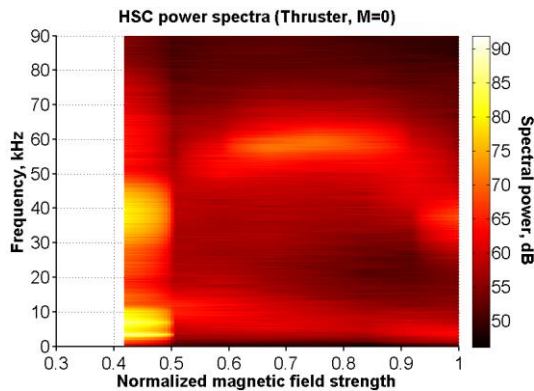


Figure 45. The $m=0$ power spectra of the thruster light intensity as magnetic field strength varied for the 400-12.5 throttle point.

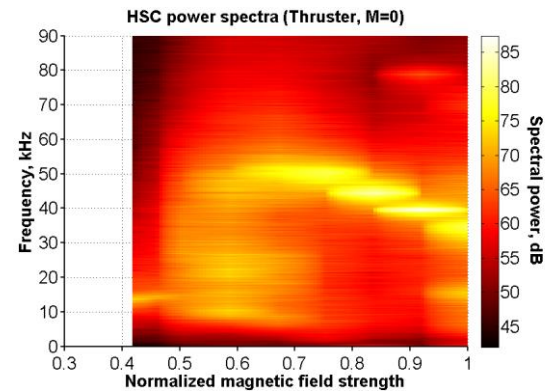


Figure 46. The $m=0$ power spectra of the thruster light intensity as magnetic field strength varied for the 500-12.5 throttle point.

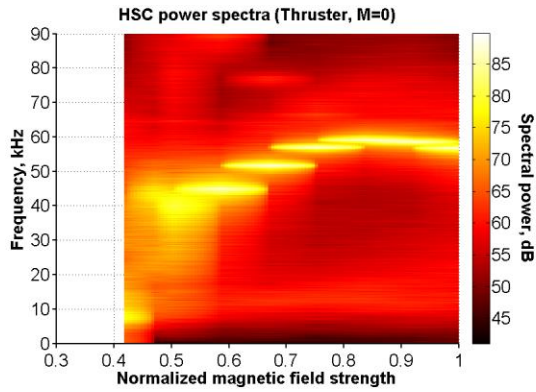


Figure 47. The $m=0$ power spectra of the thruster light intensity as magnetic field strength varied for the 600-12.5 throttle point.

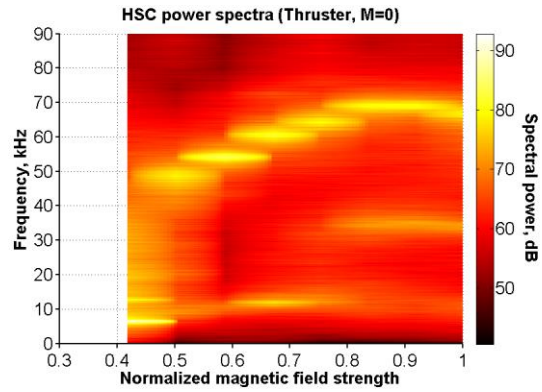


Figure 48. The $m=0$ power spectra of the thruster light intensity as magnetic field strength varied for the 700-12.5 throttle point.

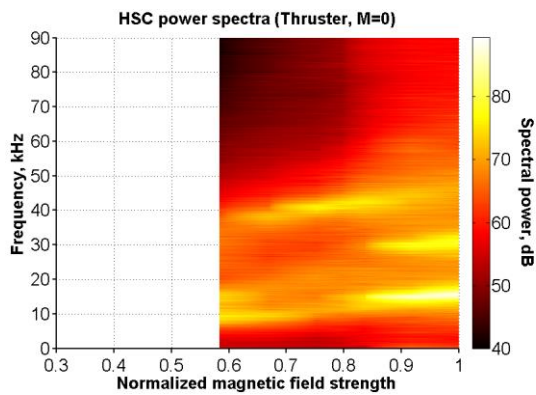


Figure 49. The $m=0$ power spectra of the thruster light intensity as magnetic field strength varied for the 800-9.7 throttle point.

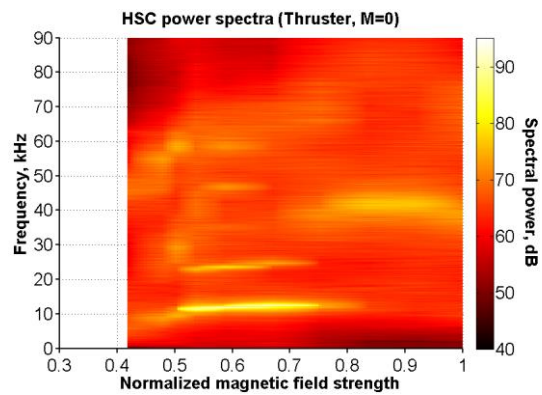


Figure 50. The $m=0$ power spectra of the thruster light intensity as magnetic field strength varied for the 800-12.5 throttle point.

Figures 51 to 58 show the contour plots of the $m = 1$ power spectra of the cathode light intensity as the magnetic field strength varied.

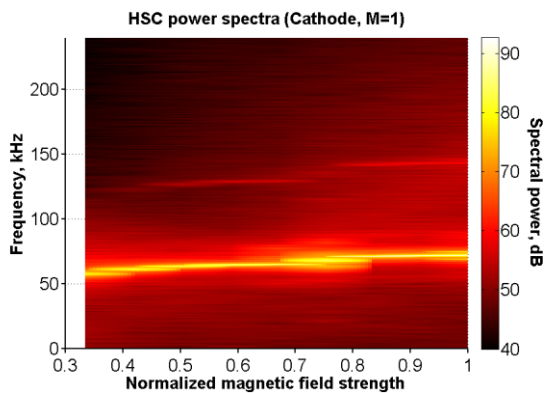


Figure 51. The $m=1$ power spectra of the cathode light intensity as magnetic field strength varied for the 300-4.7 throttle point.

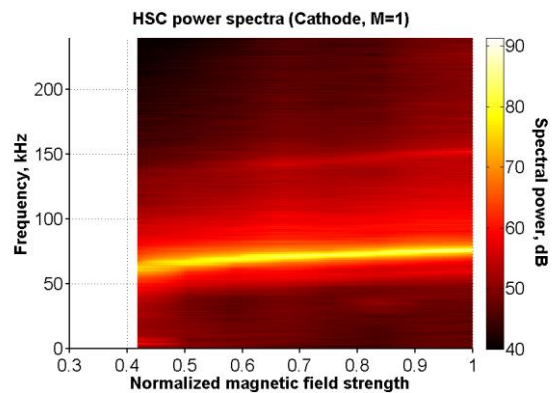


Figure 52. The $m=1$ power spectra of the cathode light intensity as magnetic field strength varied for the 300-9.4 throttle point.

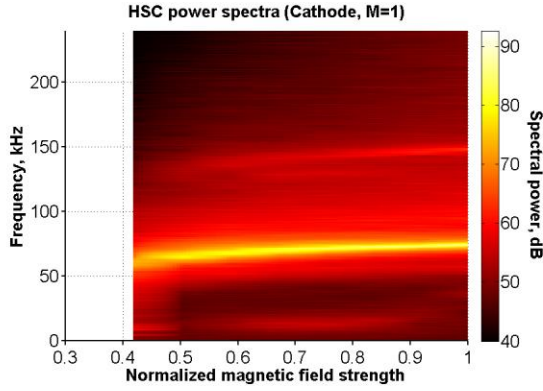


Figure 53. The $m=1$ power spectra of the cathode light intensity as magnetic field strength varied for the 400-12.5 throttle point.

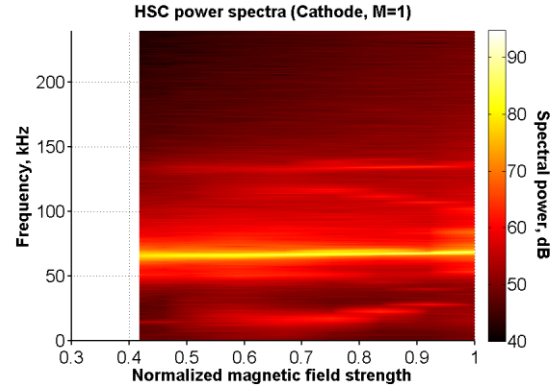


Figure 54. The $m=1$ power spectra of the cathode light intensity as magnetic field strength varied for the 500-12.5 throttle point.

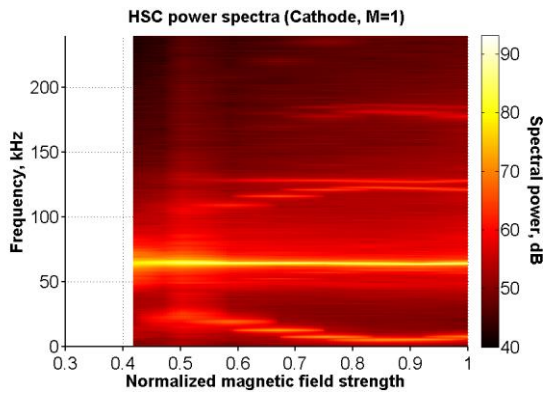


Figure 55. The $m=1$ power spectra of the cathode light intensity as magnetic field strength varied for the 600-12.5 throttle point.

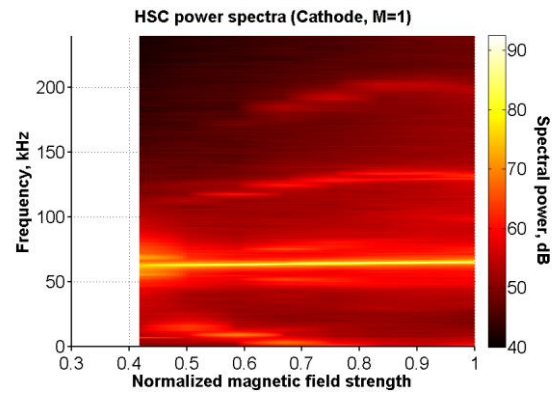


Figure 56. The $m=1$ power spectra of the cathode light intensity as magnetic field strength varied for the 700-12.5 throttle point.

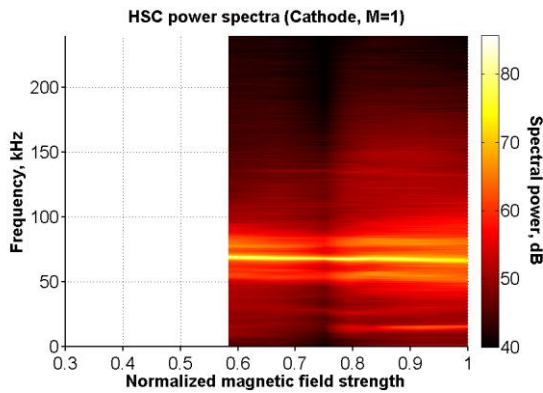


Figure 57. The $m=1$ power spectra of the cathode light intensity as magnetic field strength varied for the 800-9.7 throttle point.

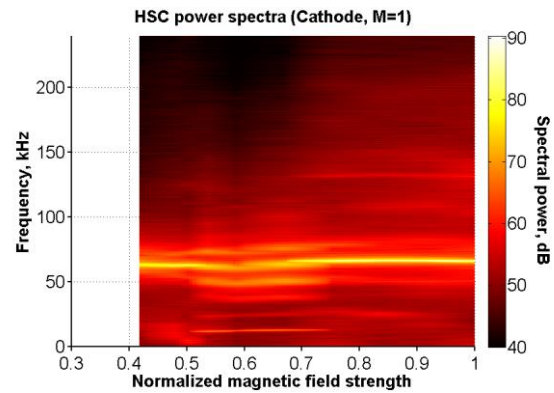


Figure 58. The $m=1$ power spectra of the cathode light intensity as magnetic field strength varied for the 800-12.5 throttle point.

Figures 59 to 62 show the contour plots of the PDFs of the thruster light intensity as the cathode flow fraction varied.

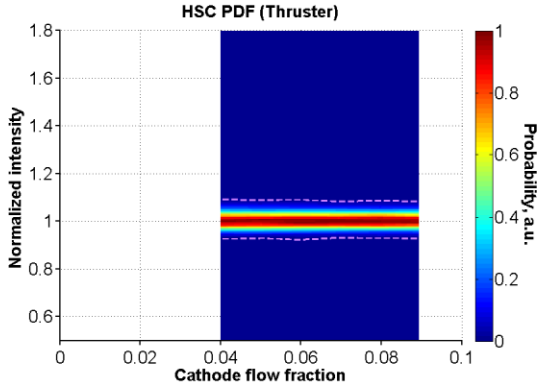


Figure 59. PDF of the thruster light intensity as cathode flow fraction varied for the 300-4.7 throttle point.

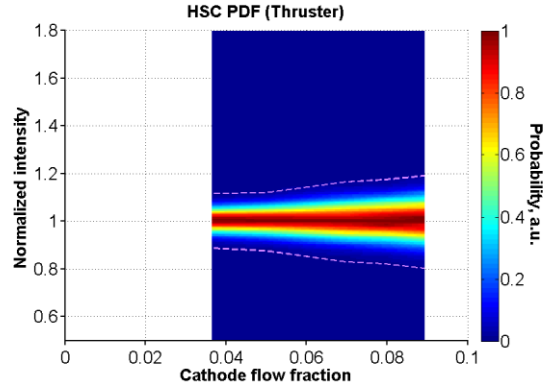


Figure 60. PDF of thruster light intensity as cathode flow fraction varied for the 300-9.4 throttle point.

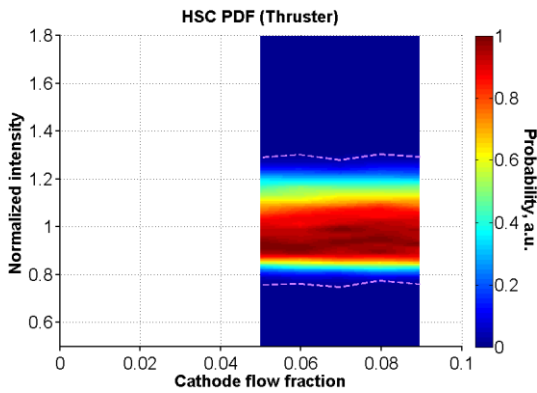


Figure 61. PDF of thruster light intensity as cathode flow fraction varied for the 800-9.7 throttle point.

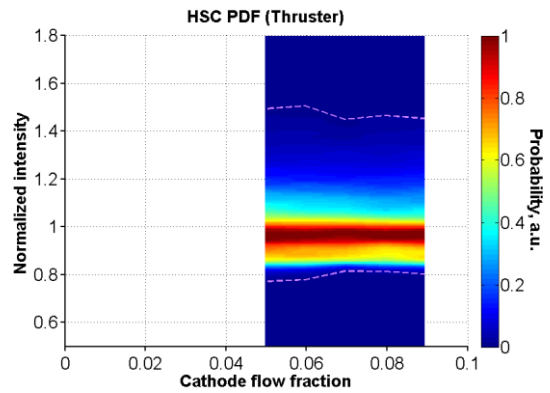


Figure 62. PDF of thruster light intensity as cathode flow fraction varied for the 800-12.5 throttle point.

Figures 63 to 66 show the contour plots of the $m = 0$ power spectra of the thruster light intensity as the cathode flow fraction varied.

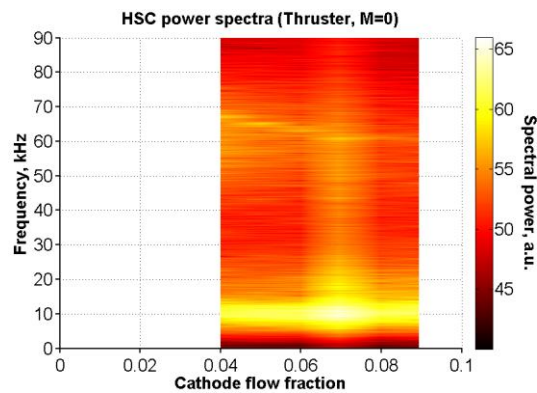


Figure 63. The $m=0$ power spectra of the thruster light intensity as cathode flow fraction varied for the 300-4.7 throttle point.

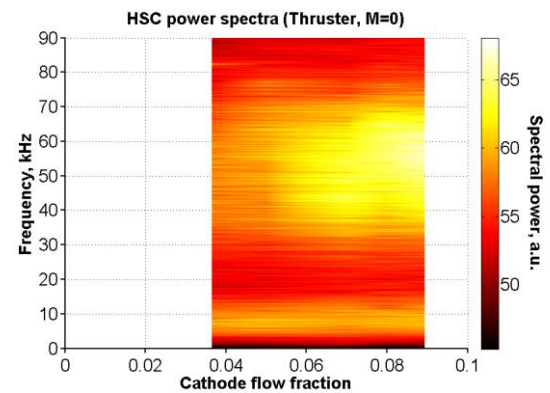


Figure 64. The $m=0$ power spectra of the thruster light intensity as cathode flow fraction varied for the 300-9.4 throttle point.

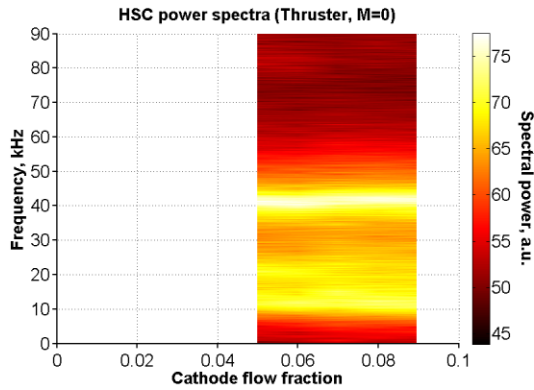


Figure 65. The $m=0$ power spectra of the thruster light intensity as cathode flow fraction varied for the 800-9.7 throttle point.

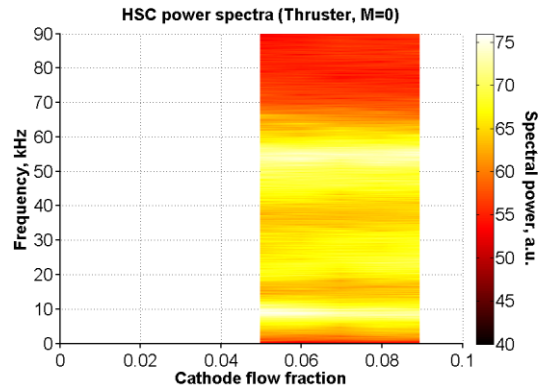


Figure 66. The $m=0$ power spectra of the thruster light intensity as cathode flow fraction varied for the 800-12.5 throttle point.

Figures 67 to 70 show the contour plots of the $m = 1$ power spectra of the cathode light intensity as the cathode flow fraction varied.

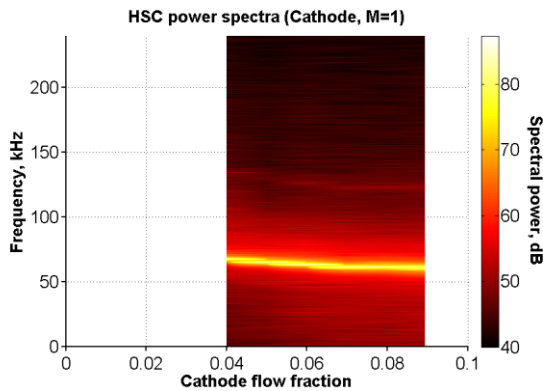


Figure 67. The $m=1$ power spectra of the cathode light intensity as cathode flow fraction varied for the 300-4.7 throttle point.

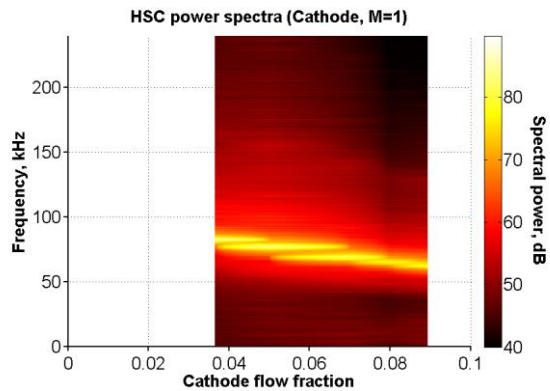


Figure 68. The $m=1$ power spectra of the cathode light intensity as cathode flow fraction varied for the 300-9.4 throttle point.

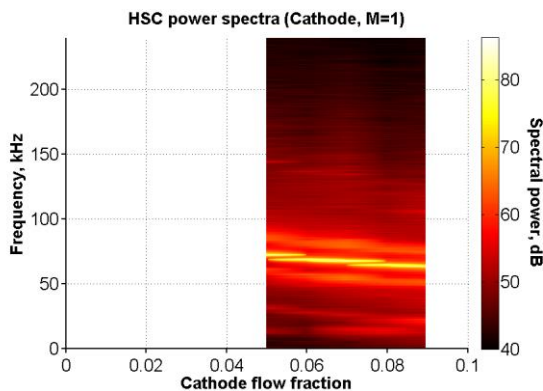


Figure 69. The $m=1$ power spectra of the cathode light intensity as cathode flow fraction varied for the 800-9.7 throttle point.

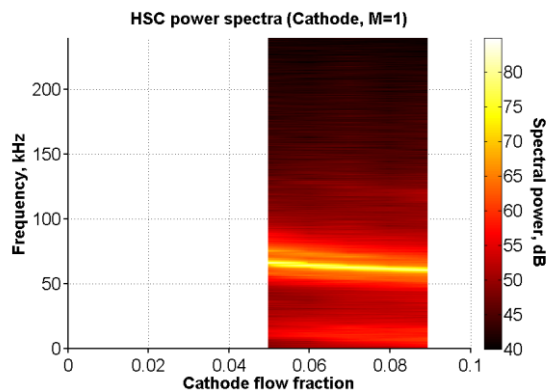


Figure 70. The $m=1$ power spectra of the cathode light intensity as cathode flow fraction varied for the 800-12.5 throttle point.

Acknowledgments

The authors would like to thank the Space Technology Mission Directorate, through the Solar Electric Propulsion Technology Demonstration Mission Project, for funding the joint NASA GRC and JPL development of the HERMeS thruster and this work. We thank the Ion Propulsion Subsystem Lead, Daniel A. Herman, and the thruster lead, Richard R. Hofer, for leading this effort. We thank Christopher M. Griffiths, John T. Yim, Lauren K. Clayman, James L. Myers, Li C. Chang, Dale A. Robinson, Peter Peterson, George Williams, James Gilland of the NASA Glenn Research Center and Ioannis Mikellides, Alejandro Lopez Ortega, Benjamin Jorns, James E. Polk, Michael J. Sekerak, Ryan Conversano of the Jet Propulsion Laboratory for work on the SEP TDM HERMeS Hall thruster. And we thank Kevin L. Blake, George P. Jacynycz, Thomas A. Ralys, and Terrell J. Jensen for the fabrication, assembly of the test setup, and operation of the vacuum facility.

References

- ¹Smith, B. K., Nazario, M. L., and Cunningham, C. C., "Solar Electric Propulsion Vehicle Demonstration to Support Future Space Exploration Missions", *Space Propulsion 2012*, Bordeaux, France, May 7-10, 2012.
- ²Manzella, D. and Hack, K., "High-Power Solar Electric Propulsion for Future NASA Missions", *50th AIAA/ASME/SAE/ASEE Joint Propulsion Conference*, AIAA-2014-3718, doi:10.2514/6.2014-3718, Cleveland, OH, Jul 28-30, 2014.
- ³Kamhawi, H., et al., "Overview of the Development of the Solar Electric Propulsion Technology Demonstration Mission 12.5-kW Hall Thruster", *50th AIAA/ASME/SAE/ASEE Joint Propulsion Conference*, AIAA-2014-3898, doi:10.2514/6.2014-3898, Cleveland, OH, Jul 28-30, 2014.
- ⁴Brophy, J. R. and Muirhead, B., "Near-Earth Asteroid Retrieval Mission (ARM) Study", *33rd International Electric Propulsion Conference*, 2013-082, Washington, DC, Oct 6-10, 2013.
- ⁵Muirhead, B. K. and Brophy, J. R., "Asteroid Redirect Robotic Mission Feasibility Study", *2014 IEEE Aerospace Conference*, doi:10.1109/AERO.2014.6836358, Big Sky, MT, Mar 1-8, 2014.
- ⁶Gates, M., et al., "NASA's Asteroid Redirect Mission Concept Development Summary", *2015 IEEE Aerospace Conference*, doi:10.1109/AERO.2015.7119163, Big Sky, MT, Mar 7-14, 2015.
- ⁷Mazanek, D. D., et al., "Asteroid Redirect Robotic Mission: Robotic Boulder Capture Option Overview", *AIAA SPACE 2014 Conference and Exposition*, AIAA-2014-4432, doi:10.2514/6.2014-4432, San Diego, CA, Aug 4-7, 2014.
- ⁸Huang, W., Yim, J. T., and Kamhawi, H., "Design and Empirical Assessment of the HERMeS Hall Thruster Propellant Manifold", *62nd Joint Army-Navy-NASA-Air Force Propulsion Meeting*, JANNAF-2015-3926, Nashville, TN, Jun 1-4, 2015.
- ⁹Shastry, R., Huang, W., and Kamhawi, H., "Near-Surface Plasma Characterization of the 12.5-kW NASA TDU1 Hall Thruster", *51st AIAA/ASME/SAE/ASEE Joint Propulsion Conference*, AIAA-2015-3919, doi:10.2514/6.2015-3919, Orlando, FL, Jul 27-29, 2015.
- ¹⁰Kamhawi, H., et al., "Performance and Facility Background Pressure Characterization Tests of NASA's 12.5-kW Hall Effect Rocket with Magnetic Shielding Thruster", *34th International Electric Propulsion Conference*, 2015-007, Kobe, Japan, Jul 4-10, 2015.
- ¹¹Huang, W., Kamhawi, H., Myers, J. L., Yim, J. T., and Neff, G., "Non-Contact Thermal Characterization of NASA's HERMeS Hall Thruster", *51st AIAA/ASME/SAE/ASEE Joint Propulsion Conference*, AIAA-2015-3920, doi:10.2514/6.2015-3920, Orlando, FL, Jul 27-29, 2015.
- ¹²Peterson, P. Y., et al., "NASA's HERMeS Hall Thruster Electrical Configuration Characterization", *52nd AIAA/ASME/SAE/ASEE Joint Propulsion Conference*, Salt Lake City, UT, Jul 25-27, 2016.
- ¹³Huang, W., Kamhawi, H., Haag, T. W., Lopez Ortega, A., and Mikellides, I. G., "Facility Effect Characterization Test of NASA's HERMeS Hall Thruster", *52nd AIAA/ASME/SAE/ASEE Joint Propulsion Conference*, Salt Lake City, UT, Jul 25-27, 2016.
- ¹⁴Choueiri, E. Y., "Plasma Oscillations in Hall Thrusters", *Physics of Plasmas*, Vol. 8, No. 4, doi:10.1063/1.1354644, Apr, 2001, pp. 1411-1426.
- ¹⁵Janes, G. S. and Lowder, R. S., "Anomalous Electron Diffusion and Ion Acceleration in a Low-Density Plasma", *Physics of Fluids*, Vol. 9, No. 6, doi:10.1063/1.1761810, 1966, pp. 1115.
- ¹⁶Morozov, A. I., Esipchuk, Y. V., Kapulkin, A. M., Nevrovskii, V. A., and Smirnov, V. A., "Effect of the Magnetic Field on a Closed-Electron-Drift Accelerator", *Soviet Physics-Technical Physics*, Vol. 17, No. 3, Sep, 1972, pp. 482-487.
- ¹⁷Esipchuk, Y. V., Morozov, A. I., Tilinin, G. N., and Trofimov, A. V., "Plasma Oscillations in Closed-Drift Accelerators with an Extended Acceleration Zone", *Soviet Physics-Technical Physics*, Vol. 18, No. 7, Jan, 1974, pp. 928-932.
- ¹⁸Esipchuk, Y. V. and Tilinin, G. N., "Drift Instability in a Hall-Current Plasma Accelerator", *Soviet Physics-Technical Physics*, Vol. 21, No. 4, Jan, 1976, pp. 417-423.
- ¹⁹Darnon, F., Lyszyk, M., and Bouchoule, A., "Optical Investigation on Plasma Oscillations of SPT Thrusters", *33rd AIAA/ASME/SAE/ASEE Joint Propulsion Conference*, AIAA-1997-3051, doi:10.2514/6.1997-3051, Seattle, WA, Jul 6-9, 1997.
- ²⁰Fife, J. M., Martinez-Sanchez, M., and Szabo, J., "A Numerical Study of Low-Frequency Discharge Oscillations in Hall Thrusters", *33rd AIAA/ASME/SAE/ASEE Joint Propulsion Conference*, AIAA-1997-3052, doi:10.2514/6.1997-3052, Seattle, WA, Jul 6-9, 1997.

- ²¹Gascon, N., et al., "Signal Processing and Non-Linear Behavior of a Stationary Plasma Thruster: First Results", *35th AIAA/ASME/SAE/ASEE Joint Propulsion Conference & Exhibit*, AIAA-1999-2427, doi:10.2514/6.1999-2427, Los Angeles, CA, Jun 20-24, 1999.
- ²²Chesta, E., Lam, C. M., Meezan, N. B., Schmidt, D. P., and Cappelli, M. A., "A Characterization of Plasma Fluctuations within a Hall Discharge", *IEEE Transactions on Plasma Science*, Vol. 29, No. 4, doi:10.1109/27.940951, Aug, 2001, pp. 582-591.
- ²³Litvak, A. A., Raites, Y., and Fisch, N. J., "Experimental Studies of High-Frequency Azimuthal Waves in Hall Thrusters", *Physics of Plasmas*, Vol. 11, No. 4, doi:10.1063/1.1634564, Apr, 2004, pp. 1701-1705.
- ²⁴Beiting, E. J., Garrett, M. L., Pollard, J. E., Pezet, B., and Gouvernayre, P., "Spectral Characteristics of Radiated Emission from SPT-100 Hall Thrusters", *29th International Electric Propulsion Conference*, 2005-221, Princeton, NJ, Oct 31-Nov 4, 2005.
- ²⁵Lobbia, R. B., "A Time-resolved Investigation of the Hall Thruster Breathing Mode", Ph.D. Dissertation, Aerospace Engineering, University of Michigan, Ann Arbor, MI, 2009.
- ²⁶Nakles, M. R. and Hargus, W. A., Jr., "Background Pressure Effects on Ion Velocity Distribution Within a Medium-Power Hall Thruster", *Journal of Propulsion and Power*, Vol. 27, No. 4, doi:10.2514/1.48027, Jul-Aug, 2011, pp. 737-743.
- ²⁷McDonald, M. S., "Electron Transport in Hall Thrusters", Ph.D. Dissertation, Aerospace Engineering, University of Michigan, Ann Arbor, MI, 2012.
- ²⁸Sekerak, M. J., "Plasma Oscillations and Operational Modes in Hall Effect Thrusters", Ph.D. Dissertation, Aerospace Engineering, University of Michigan, Ann Arbor, MI, 2014.
- ²⁹Hara, K., Sekerak, M. J., Boyd, I. D., and Gallimore, A. D., "Mode transition of a Hall thruster discharge plasma", *Journal of Applied Physics*, Vol. 115, No. 20, doi:10.1063/1.4879896, May 29, 2014, pp. 203304.
- ³⁰Sekerak, M. J., et al., "Mode Transitions in Magnetically Shielded Hall Effect Thrusters", *50th AIAA/ASME/SAE/ASEE Joint Propulsion Conference*, AIAA-2014-3511, doi:10.2514/6.2014-3511, Cleveland, OH, Jul 28-30, 2014.
- ³¹Jorns, B. A. and Hofer, R. R., "Plasma oscillations in a 6-kW magnetically shielded Hall thruster", *Physics of Plasmas*, Vol. 21, No. 5, doi:10.1063/1.4879819, May 30, 2014, pp. 053512.
- ³²Yim, J. T. and Burt, J. M., "Characterization of Vacuum Facility Background Gas Through Simulation and Considerations for Electric Propulsion Ground Testing", *51st AIAA/ASME/SAE/ASEE Joint Propulsion Conference*, AIAA-2015-3825, doi:10.2514/6.2015-3825, Orlando, FL, Jul 27-29, 2015.
- ³³Huang, W., Kamhawi, H., Lobbia, R. B., and Brown, D. L., "Effect of Background Pressure on the Plasma Oscillation Characteristics of the HiVHAc Hall Thruster", *50th AIAA/ASME/SAE/ASEE Joint Propulsion Conference*, AIAA-2014-3708, doi:10.2514/6.2014-3708, Cleveland, OH, Jul 28-30, 2014.
- ³⁴Herman, D. A., et al., "The Ion Propulsion System for the Asteroid Redirect Robotic Mission", *52nd AIAA/ASME/SAE/ASEE Joint Propulsion Conference*, Salt Lake City, UT, Jul 25-27, 2016.